iScience

CellPress
OPEN ACCESS

Article

Potassium ions promote hexokinase-II dependent glycolysis

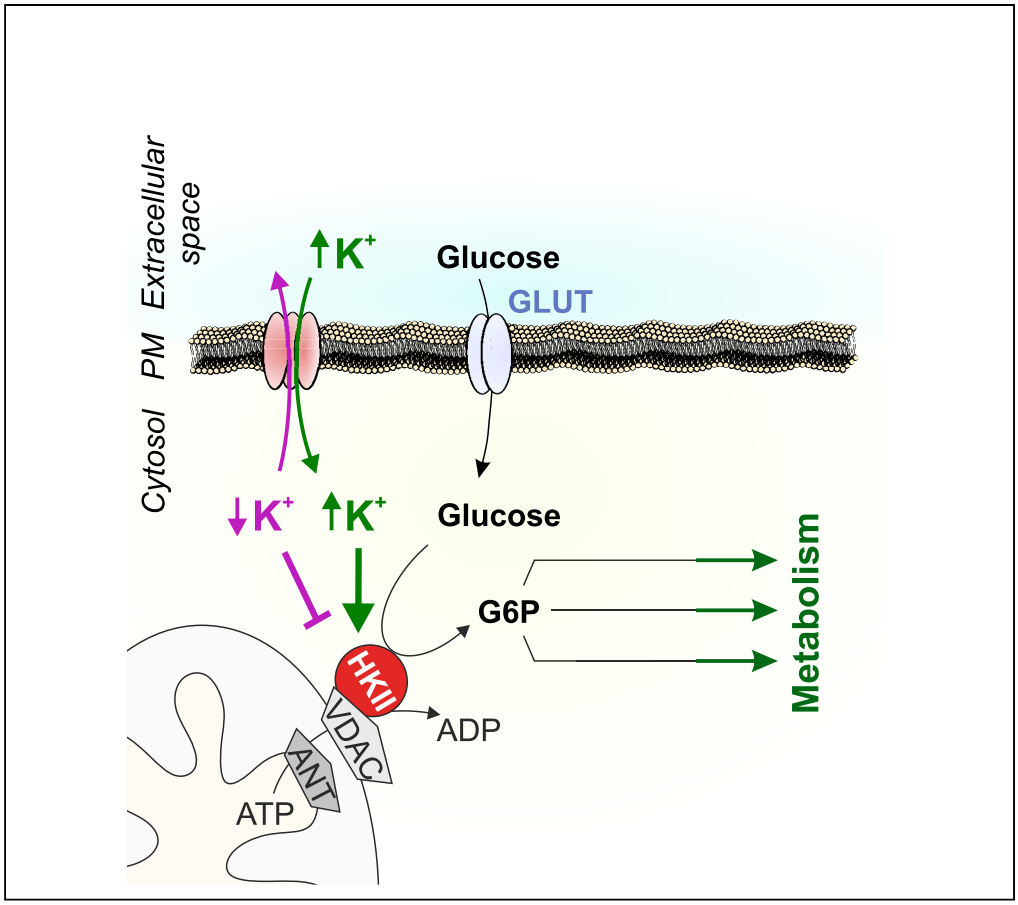

Helmut Bischof, Sandra Burgstaller, Anna Springer, ..., Robert Lukowski, Wolfgang F. Graier, Roland Malli

helmut.bischof@uni-tuebingen.de (H.B.)
roland.malli@medunigraz.at (R.M.)

Highlights

HKII expression sensitizes cellular metabolism for intracellular K

Intracellular K^+ depletion abates the metabolic activity of HKII-positive cells

(Re-)elevations of intracellular K^+ restore glycolysis

Bischof et al., iScience *24*, 102346
April 23, 2021
https://doi.org/10.1016/j.isci.2021.102346

iScience

CellPress
OPEN ACCESS

Article

Potassium ions promote hexokinase-II dependent glycolysis

Helmut Bischof,[1,2,8,*] Sandra Burgstaller,[1,3] Anna Springer,[1] Lucas Matt,[2] Thomas Rauter,[1] Olaf A. Bachkönig,[1] Tony Schmidt,[4] Klaus Groschner,[4,5] Rainer Schindl,[4,5] Tobias Madl,[1,5] Nikolaus Plesnila,[6,7] Robert Lukowski,[2] Wolfgang F. Graier,[1,5] and Roland Malli[1,5,*]

SUMMARY

High expression levels of mitochondria-associated hexokinase-II (HKII) represent a hallmark of metabolically highly active cells such as fast proliferating cancer cells. Typically, the enzyme provides a crucial metabolic switch towards aerobic glycolysis. By imaging metabolic activities on the single-cell level with genetically encoded fluorescent biosensors, we here demonstrate that HKII activity requires intracellular K^+. The K^+ dependency of glycolysis in cells expressing HKII was confirmed in cell populations using extracellular flux analysis and nuclear magnetic resonance-based metabolomics. Reductions of intracellular K^+ by gramicidin acutely disrupted HKII-dependent glycolysis and triggered energy stress pathways, while K^+ re-addition promptly restored glycolysis-dependent adenosine-5′-triphosphate generation. Moreover, expression and activation of $K_V1.3$, a voltage-gated K^+ channel, lowered cellular K^+ content and the glycolytic activity of HEK293 cells. Our findings unveil K^+ as an essential cofactor of HKII and provide a mechanistic link between activities of distinct K^+ channels and cell metabolism.

INTRODUCTION

Cellular glucose uptake and the subsequent phosphorylation of glucose via hexokinase (HK) isoforms represent the initial and crucial step in glucose metabolism. From four different HK isoforms identified, hexokinase-I (HKI) and hexokinase-II (HKII) represent isoforms that are capable of associating with the voltage-dependent anion channel (VDAC) located at the outer mitochondrial membrane. The localization of HK isoforms at the surface of mitochondria facilitates adenosine-5′-triphosphate (ATP) supply of the enzymes and additionally protects cells from apoptosis (Abu-Hamad et al., 2008; Gottlob, 2001; Mathupala et al., 2009; Roberts and Miyamoto, 2015). Moreover, especially HKII, which is highly expressed in most cancer cells and has been shown to drive tumor initiation and progression in murine cancer models, is frequently associated with high cell metabolic activities (Anderson et al., 2017; Mathupala et al., 2006). Remarkably, potassium ions (K^+), the most abundant intracellular cations (Palmer, 2015), exert a stabilizing effect on purified HKII *in vitro*, thereby preventing the thermal inactivation of the enzyme (Rose and Warms, 1982). Besides the high expression rate of cancer-associated HKII, cancer onset and progression are frequently associated with altered expression and activity of certain K^+ channels that control and modulate abnormal cell proliferation (Huang and Jan, 2014; Mathupala et al., 2006; Mohr et al., 2020). Accordingly, pharmacological tools impairing the (sub-)cellular K^+ homeostasis have shown potent anticancer properties *in vitro* and animal models. Interestingly, the activation of specific K^+ channels or the inhibition of the sodium ion (Na^+)/K^+ adenosine triphosphatase represents effective anticancer and senolytic strategies (Guerrero et al., 2019; Lansu and Gentile, 2013; Sanderson et al., 2020; Steudel et al., 2017; Triana-Martínez et al., 2019). However, despite these known implications of targeting the cellular K^+ homeostasis on (cancer) cell viability, the underlying mechanism mediating the cell death induction remains largely enigmatic. By exploiting single-cell imaging approaches to visualize subcellular ATP, glucose, K^+, and lactate concentrations and dynamics, we here unveil that depletions of $[K^+]_i$ reduce glycolysis and ATP generation in cells expressing HKII. Extracellular flux analysis of acidification and oxygen consumption and NMR metabolomics confirmed that HKII requires intracellular K^+ for its full catalytic activity.

[1]Gottfried Schatz Research Center, Molecular Biology and Biochemistry, Medical University of Graz, Neue Stiftingtalstraße 6/6, 8010 Graz, Austria

[2]Department of Pharmacology, Toxicology and Clinical Pharmacy, Institute of Pharmacy, University of Tuebingen, Auf der Morgenstelle 8, 72076 Tuebingen, Germany

[3]Department of Molecular Biology, Interfaculty Institute for Cell Biology, University of Tuebingen, Auf der Morgenstelle 15, 72076 Tuebingen, Germany

[4]Gottfried Schatz Research Center, Biophysics, Medical University of Graz, Neue Stiftingtalstraße 6/6, 8010 Graz, Austria

[5]BioTechMed-Graz, Mozartgasse 12/II, 8010 Graz, Austria

[6]Laboratory of Experimental Stroke Research, Institute for Stroke and Dementia Research, University of Munich Medical Center, Munich, Germany

[7]Munich Cluster for Systems Neurology (SyNergy), Munich, Germany

[8]Lead contact

*Correspondence: helmut.bischof@uni-tuebingen.de (H.B.), roland.malli@medunigraz.at (R.M.)

https://doi.org/10.1016/j.isci.2021.102346

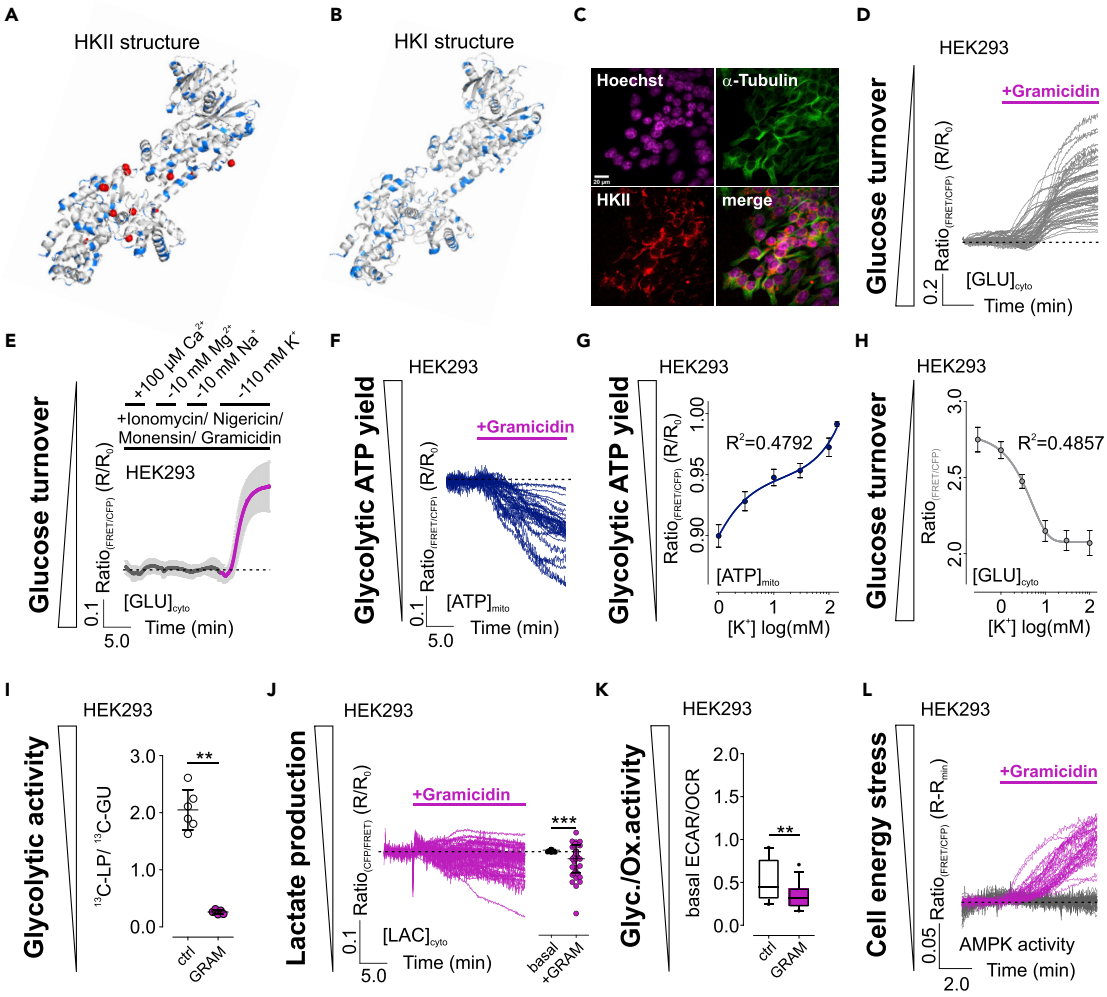

Figure 1. Intracellular K^+ depletion induces disturbances of cellular energy homeostasis in HEK293 cells.

(A and B) HKII (A) and HKI (B) structure with potential K^+ binding amino acids in blue and unknown atoms or ions found in the crystallographic model of HKII in red.

(C) IF images of HEK293 cells. Scale bar shows 20 µm, n = 7.

(D) $[GLU]_{cyto}$ over-time of single HEK293 cells in response to gramicidin. n = 4.

(E) Average $[GLU]_{cyto}$ over-time ± standard deviation (SD) of HEK293 cells kept in a cytosol-like buffer and an ionophore mixture. Ions were added or removed as indicated. n = 4.

(F) $[ATP]_{mito}$ responses of single HEK293 cells in response to gramicidin. n = 4.

(G and H) $[ATP]_{mito}$ (G) and $[GLU]_{cyto}$ (H) over $[K^+]$. Both panels show average ± standard error of mean of 3 independent experiments.

(I) ^{13}C-lactate production (LP)/^{13}C-glucose uptake (GU) ratio of HEK293 cells either treated with DMSO (ctrl, white) or gramicidin (GRAM, magenta). Data represent each replicate and average ± SD. n = 6, $^{**}p \leq 0.01$, Mann-Whitney test.

(J) $[LAC]_{cyto}$ over-time (left) and statistics (right) of HEK293 cells treated with gramicidin. Single cell responses and average ± SD are shown, $^{***}p \leq 0.001$, Wilcoxon matched-pairs signed rank test, n = 4.

(K) ECAR/OCR ratios of HEK293 cells treated with DMSO (ctrl) or gramicidin (GRAM). $^{**}p \leq 0.01$, Mann-Whitney test. n = 4. Boxes indicate the median and the first and third quartile. Lower and upper whiskers indicate 5-95 percentile; outliers are indicated as black dots.

(L) Responses of single HEK293 cells expressing AMPKAR upon DMSO (grey) or gramicidin (magenta) treatment. n = 3.

See also Figures S1 and S2.

RESULTS

Low $[K^+]$ impair HKII activity *in vitro* and aerobic glycolysis in cells

First, using the purified enzyme, we confirmed that high $[K^+]$ counteract the thermal inactivation of HKII with an EC_{50} of 18.98 (7.12–50.56) mM K^+ (Figure S1A). Under these conditions, the enzymatic activity of HKI was not significantly affected (Figure S1B). To substantiate, whether K^+ could directly affect HKII enzymatic activity, we investigated a crystallographic model of HKII (Figure 1A) (Nawaz et al., 2018). This analysis

revealed several unidentified atoms or ions being near to amino acids known to feature strong K^+ binding (Figure 1A) (Heaton and Armentrout, 2008). Such unidentified atoms or ions were absent in a crystallographic model of HKI (Figure 1B) (Rosano et al., 1999). Analysis of the protein sequences of HKI and HKII unveiled a high homology of the full-length protein sequences of the two HK isoforms of ~73.4% (Figure S1C). Further in-depth analysis of the potential amino acids interacting with the unidentified atoms in HKII demonstrated four positions of potential interaction that were different in HKII compared to HKI, comprising the amino acid transitions N89S, H422Q and K425R, Q471E and E821T, and E724H from HKII to HKI, respectively (Figure S1D). Interestingly, in three of the four positions, amino acids featuring strong K^+ binding (Heaton and Armentrout, 2008) were found in HKII but not HKI. Also, the homology of HKI and HKII was reduced to ~65.7% in regions 10 amino acids upstream and downstream of the potential interaction sites. Non-homologous amino acids in these regions frequently comprised strongly K^+ binding amino acids (Figures S1C and S1D). We hypothesized that these positions, which are additionally found close to the protein surface (Figure S1E), could sensitize HKII for K^+.

To elucidate, whether K^+ controls HKII activity also in its cellular environment, we aimed to manipulate $[K^+]_i$. We proved its efficiency using K^+ biosensors (Bischof et al., 2017) expressed in different human cell lines including HEK293 (human embryonic kidney cells) and the cancer cell lines HeLa (human cervical cancer cells), INS-1 832/13 (a rat insulinoma cell line), MCF-7, and MDA-MB-453 (human breast cancer cell lines). Administration of gramicidin efficiently lowered cytosolic (Figure S2A) and mitochondrial $[K^+]$ ($[K^+]_{cyto}$, $[K^+]_{mito}$) (Figure S2B), respectively, within few minutes in all cell types tested. We next monitored the cytosolic glucose concentration ($[GLU]_{cyto}$) over-time as a measure of glycolytic activity, using a fluorescence resonance energy transfer (FRET)-based glucose sensor (Bermejo et al., 2010), while depleting $[K^+]_i$ in HEK293 cells, as these cells show high endogenous HKII expression levels (Figure 1C) (Peng et al., 2008). $[K^+]_i$ reduction yielded immediate elevations of $[GLU]_{cyto}$ (Figure 1D), indicating hampered glucose phosphorylation, causing an increase of $[GLU]_{cyto}$ due to ongoing glucose import in HEK293 cells, when intracellular K^+ is depleted. To scrutinize a potential role of other physiologically relevant metal ions (Bischof et al., 2019), we permeabilized HEK293 cells using a mixture of different ionophores and gramicidin, followed by manipulating the concentrations of calcium (Ca^{2+}), magnesium (Mg^{2+}), sodium (Na^+) ions, and K^+, respectively (Figure 1E). These experiments unveiled that solely K^+ removal induced a pronounced increase of $[GLU]_{cyto}$ in HKII-expressing HEK293 cells, supporting the idea of a K^+-modulated HKII activity.

We next monitored the mitochondrial concentration of adenosine-5′-triphosphate ($[ATP]_{mito}$) using an approved ATP biosensor targeted to the mitochondrial matrix (Imamura et al., 2009). $[K^+]_i$ depletion reduced $[ATP]_{mito}$ over-time in HEK293 cells (Figure 1F), similar to extracellular glucose removal (Figure S2C). These results imply the necessity of high $[K^+]_i$ for maintaining $[ATP]_{mito}$ supply and glycolytic activity in HEK293 cells.

To estimate the sensitivity of cell metabolism for K^+, we analyzed $[GLU]_{cyto}$ and $[ATP]_{mito}$ in HEK293 cells upon their permeabilization with gramicidin in the presence of different $[K^+]_{ex}$. $[K^+]_{cyto}$ strictly followed $[K^+]_{ex}$ as measured by NES lc-LysM GEPII 1.0 (Figure S2D), again indicating the suitability of gramicidin to freely manipulate $[K^+]_{cyto}$. Next, we analyzed $[ATP]_{mito}$ under these conditions. These experiments unveiled a decrease of $[ATP]_{mito}$, which well correlated with decreasing $[K^+]_{cyto}$ (Figures 1G and S2E). As expected, $[ATP]_{mito}$ of gramicidin-treated HEK293 cells decreased in a $[K^+]$-dependent manner (Figures 1G and S2E). Thereby, the decrease of $[ATP]_{mito}$ upon decreasing $[K^+]_{cyto}$ seemed biphasic, which would indicate multiple K^+ binding sites with different affinities of HKII (Figures 1G and S2E). The sensitivities of $[ATP]_{mito}$ for K^+ were observed at a half-maximal effective concentration (EC_{50}) of ~3.0 mM K^+ and a second EC_{50} of ≥70.0 mM (Figure 1G). Similar results were obtained by analyzing $[GLU]_{cyto}$ in a HEK293 cell population upon gramicidin treatment in the presence of distinct $[K^+]_{ex}$, which also unveiled an EC_{50} of $[GLU]_{cyto}$ for K^+ of 3.63 mM (2.12 mM–6.23 mM) (Figure 1H). Under these conditions, a second EC_{50} could not be determined yet (Figure 1H). Together, these data indicate that the full depletion of $[ATP]_{mito}$ and maximal accumulation of $[GLU]_{cyto}$ requires a strong intracellular K^+ depletion. Nevertheless, our analysis also indicates that physiological intracellular K^+ fluctuations in the higher mM range might modulate HKII-dependent cell metabolic activity.

We further analyzed the lactate production (LP)/glucose uptake (GU) ratio of HEK293 cells by NMR metabolomics. These experiments confirmed the importance of $[K^+]_i$ for aerobic glycolysis in HEK293 cells, as LP/GU ratio significantly decreased in cells treated with gramicidin for a depletion of $[K^+]_i$ compared to intact control cells (Figure 1I). The decline of cytosolic lactate concentrations ($[LAC]_{cyto}$) upon lowering $[K^+]_i$ in

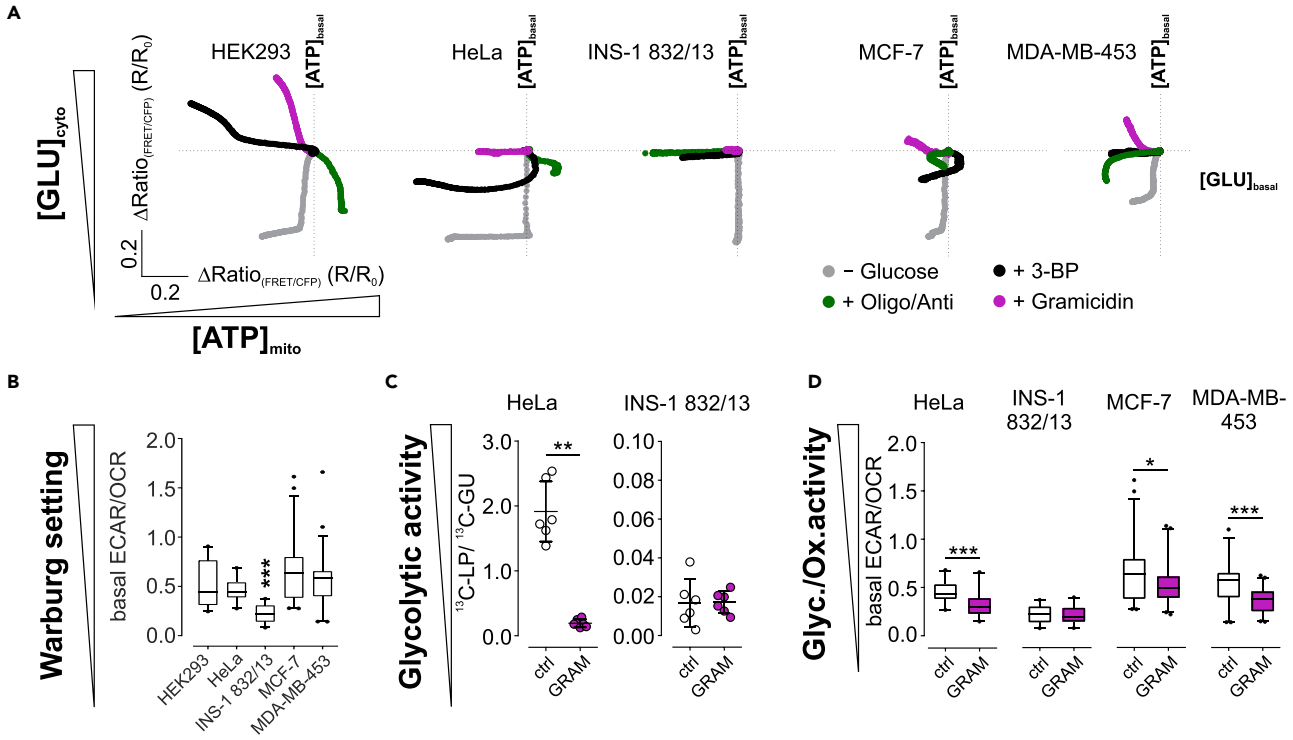

Figure 2. Intracellular K^+ depletion affects energy homeostasis in cells with a metabolic Warburg setting.

(A) Average $[GLU]_{cyto}$ and $[ATP]_{mito}$ of different cell lines upon metabolic interventions as indicated, n ≥ 3.

(B) Basal ECAR/OCR ratios of different cell lines. High ratios indicate the metabolic Warburg setting. Boxes indicate the median and the first and third quartile. Lower and upper whiskers indicate 5-95 percentile; outliers are indicated as black dots. n = 4 for all. ***p ≤ 0.001, Friedman test followed by Dunn's MC test.

(C) ^{13}C-lactate production (LP)/^{13}C-glucose uptake (GU) ratio of HeLa and INS-1 832/13 cells either treated with DMSO (ctrl, white) or gramicidin (GRAM, magenta). Data represent each replicate and average ± standard deviation. n = 6, **p ≤ 0.01, Mann-Whitney test.

(D) ECAR/OCR ratios of different cell lines treated with DMSO (ctrl, white) or gramicidin (GRAM, magenta). Boxes indicate the median and the first and third quartile. Lower and upper whiskers indicate 5-95 percentile; outliers are indicated as black dots. *p ≤ 0.05, ***p ≤ 0.001, Mann-Whitney test. n = 4 for all. See also Figure S2.

HEK293 cells was also observed using a lactate biosensor (San Martín et al., 2013) (Figure 1J). Extracellular flux analysis confirmed a reduced glycolytic activity of HEK293 cells by low $[K^+]_i$ (Figure 1K). In line with our expectations, the analysis of adenosine monophosphate-activated protein kinase (AMPK) activity, a central cell energy stress sensor (Hardie et al., 2012; Najafov et al., 2020), using an AMPK activity reporter (Tsou et al., 2011), revealed increasing AMPK activity upon reducing $[K^+]_i$ in HEK293 cells (Figure 1L), confirming the induction of energy stress by cellular K^+ depletion. Altogether, our results indicate an abated aerobic glycolysis activity when $[K^+]_i$ is low in HKII-expressing HEK293 cells (Figure S2F).

K^+ controls glycolysis in (cancer) cell lines with a Warburg setting

We further aimed to identify, whether $[K^+]_i$ also modulates the metabolism of other (cancer) cell lines. Therefore, we assessed $[GLU]_{cyto}$ and $[ATP]_{mito}$ upon lowering $[K^+]_i$ in HeLa, INS-1 832/13, MCF-7, and MDA-MB-453 cells (Figures 2A, S2G, and S2H). Interestingly, we observed declining $[ATP]_{mito}$ in all cell lines tested, except INS-1 832/13 cells, and increasing $[GLU]_{cyto}$ in HEK293, MCF-7 and MDA-MB-453, while $[GLU]_{cyto}$ remained unaffected in HeLa and INS-1 832/13 cells upon gramicidin administration (Figure 2A). Besides cell treatment with gramicidin for depleting $[K^+]_i$, we tested other metabolic interventions, including the removal of extracellular glucose, the depolarization of mitochondria, or inhibition of HKII by 3-bromo-2-oxopropionic acid (3-BP) (Figure 2A). Interestingly, the effect of depleting $[K^+]_i$ on $[GLU]_{cyto}$ and $[ATP]_{mito}$ differed from all other metabolic interventions in all cell lines, confirming their differential nutrient requirements (Figure 2A). Thereby, high $[K^+]_i$ is essential for maintaining energy homeostasis in cells with a Warburg setting (Figures 2A and 2B), as also confirmed by NMR metabolomics and extracellular flux analysis. While LP/GU ratio decreased in HeLa cells (Figure 2C) and ECAR/OCR ratio decreased in HeLa, MCF-7, and MDA-MB-453 cells upon reducing $[K^+]_i$ (Figure 2D), LP/GU ratio and ECAR/OCR ratio

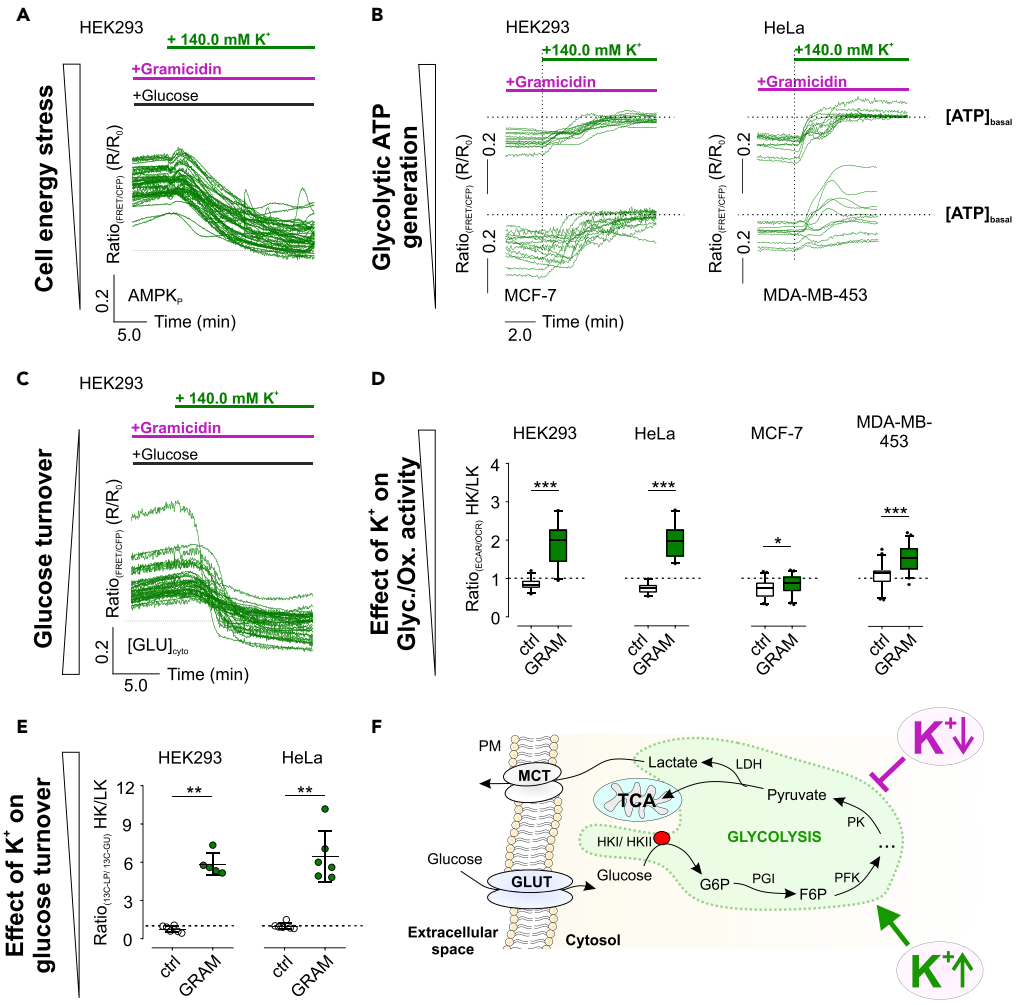

Figure 3. Restoring high $[K^+]_i$ restores aerobic glycolysis.

(A) HEK293 cells expressing AMPKAR were analyzed upon glucose removal and gramicidin pre-treatment. At the time point indicated, $[K^+]_{ex}$ was increased from 0 mM to 140.0 mM. n = 4.

(B) $[ATP]_{mito}$ over-time of gramicidin-treated cells upon addition of 140.0 mM K^+ as indicated. n ≥ 3 for all.

(C) $[GLU]_{cyto}$ over-time of HEK293 cells pre-stimulated with gramicidin in the presence of glucose and the absence of K^+. At the time point indicated, 140.0 mM K^+ was added. n = 3.

(D and E) (D) 140.0 mM K^+ (HK)/0 mM K^+ (LK) ECAR/OCR ratios and (E) HK/LK ^{13}C-LP/^{13}C-GU ratios of cells treated with DMSO (ctrl, white) or gramicidin (GRAM, green). Data are either represented as boxes with 5-95 percentile and outliers as black dots (D) or each replicate and average ± standard deviation (E). n = 4 for (D) and n ≥ 5 for (E).

(F) Simplified illustration of K^+-modulated glycolysis.

See also Figure S3.

remained unaffected in INS-1 832/13 cells (Figures 2C and 2D), possessing the high oxidative and low glycolytic activity typical for an anti-Warburg setting (Figure 2B).

Restoring high $[K^+]_i$ instantly re-establishes glucose metabolism

Our subsequent experiments aimed to identify the reversibility of the reduced metabolic activity upon $[K^+]_i$ depletion. Both $[K^+]_{cyto}$ (Figure S3A) and $[K^+]_{mito}$ (Figure S3B) were restored within minutes upon extracellular re-addition of 140.0 mM K^+. Restoring high $[K^+]_i$ resulted in a recovery of AMPK activity (Figure 3A), $[ATP]_{mito}$ (Figure 3B), and $[GLU]_{cyto}$ (Figure 3C) in all cell lines investigated. The rescue of the metabolic activity was furthermore confirmed by extracellular flux analysis (Figures 3D, S3C, and S3D) and NMR metabolomics (Figures 3E and S3E–S3G), while INS-1 832/13 cells remained again unaffected (Figures S3H–S3M). In sum, our data demonstrate that glucose metabolism is re-established by restoring high $[K^+]_i$ (Figure 3F).

$[K^+]_i$ is required for full glycolytic activity

We next investigated whether the K^+ dependency of glycolysis is also given when mitochondria are depolarized. Interestingly, the inhibition of mitochondrial respiration drastically reduced $[GLU]_{cyto}$ in the strongly glycolytically active cell lines HEK293 (Figure 4A) and HeLa (Figure 4B), eventually due to increasing glycolytic (Figure S4A) and decreasing respiratory activity (Figure S4B). Glucose removal reduced $[GLU]_{cyto}$ (Figures 4A and 4B), which remained low upon glucose re-addition, suggesting that glucose turnover rates exceed the velocity of glucose uptake. Strikingly, also under these conditions, a lowering of $[K^+]_i$ induced strong $[GLU]_{cyto}$ accumulation (Figures 4A and 4B), emphasizing that $[K^+]_i$ depletion also abolishes propelled glucose turnover (Figure S4C).

We next analyzed $[ATP]_{mito}$ of HeLa cells upon treatment with mannose (Figure S4D), a hexose sugar that is phosphorylated by HKs to mannose-6-phosphate (M6P) but is not further processed to generate ATP within this cell type. As observed earlier (Depaoli et al., 2018), mannose addition rapidly reduced $[ATP]_{mito}$ due to active ATP consumption by HKs and the lack of ATP *de novo* synthesis (Figures 4C, S4E, and S4F). $[ATP]_{mito}$ transiently increased upon mannose removal from control cells (Figures S4E and S4F), possibly due to mitochondrial HKs catalyzing the reverse reaction, thereby generating ATP from M6P and adenosine-5′-diphosphate (Depaoli et al., 2018), while $[K^+]_i$-depleted cells did not show $[ATP]_{mito}$ elevations until $[K^+]_i$ was restored (Figures 4C and S3F). These results also confirm a K^+ dependency of HKII in HeLa cells.

HKI and HKII expression levels determine the $[K^+]_i$ sensitivity of glucose metabolism

To investigate whether the K^+ sensitivity of glucose metabolism correlates with the HK expression, we manipulated the HKI/HKII ratio of HEK293, HeLa, and INS-1 832/13 cells, showing highly differential HK expression patterns (Figures 4D–4F). To this end, treatment with siRNAs against HKI or HKII, respectively, strongly reduced their expression levels in HEK293 cells (Figure S4G). Next, we analyzed $[GLU]_{cyto}$ and $[ATP]_{mito}$ of HEK293 cells treated with the different siRNAs. We found higher basal $[GLU]_{cyto}$ upon knockdown of HKII compared to HKI (Figure 4G). $[K^+]_i$ depletion increased $[GLU]_{cyto}$ in siHKI-treated cells, while the effect was reduced in siHKII-treated HEK293 cells (Figure 4G). Re-addition of high K^+ reduced $[GLU]_{cyto}$ to basal levels, and glucose removal depleted $[GLU]_{cyto}$ under both conditions (Figure 4G). The potential K^+-sensitive activity of HKII was confirmed by analyzing $[ATP]_{mito}$ under these conditions (Figures S4H–S4K). Interestingly, treatment of HEK293 cells with siHKII yielded lower basal $[ATP]_{mito}$ compared to siHKI (Figures S4H–S4J). Administration of gramicidin strongly depleted $[ATP]_{mito}$ of siHKI, but to a lesser extent of siHKII-treated HEK293 cells (Figure S4K). Restoring $[K^+]_i$ re-established basal $[ATP]_{mito}$ (Figures S4H and S4I). Altogether, these findings strongly point to a K^+-sensitive activity of HKII in HEK293 cells.

Vice versa, we addressed whether increasing HKII levels introduce a K^+-sensitive glucose utilization. Therefore, we expressed HKI-mRuby3 or HKII-mRuby3 (Figure S4K) in HeLa and INS-1 832/13 cells (Figure S4L), respectively. Indeed, $[GLU]_{cyto}$ of HeLa (Figure 4H) and INS-1 832/13 cells (Figure 4I) expressing HKII-mRuby3 were lower compared to cells expressing HKI-mRuby3 under resting conditions. Expression of HKII-mRuby3, but not HKI-mRuby3, sensitized $[GLU]_{cyto}$ of both cell lines for $[K^+]_i$ (Figures 4H and 4I), indicating that solely HKII mediates the K^+ sensitivity of cell metabolism.

Mitochondrial localization of HKII is required for its K^+ sensitivity

To further investigate whether the mitochondrial association of HKII is required for its K^+ sensitive activity, we expressed a truncated HKII-GFP (trHKII-GFP) variant lacking the first 21 amino acids (Figure S4M), which encode for the N-terminal mitochondrial binding domain (Sun et al., 2008). As expected, trHKII-EGFP was found throughout the cytosol of HeLa cells expressing the construct (Figure S4M). We further aimed to identify whether also the expression of trHKII-GFP could sensitize $[GLU]_{cyto}$ of HeLa cells to alterations of $[K^+]$, as observed for the full-length construct (Figure 4H). Interestingly, basal $[GLU]_{cyto}$ of HeLa cells expressing trHKII was similar to wild-type HeLa cells (Figure 5A). Neither the administration of gramicidin in the absence of $[K^+]_{ex}$ nor the re-addition of 140.0 mM K^+ significantly affected $[GLU]_{cyto}$ of WT or trHKII-EGFP-expressing HeLa cells (Figure 5A). Removal of extracellular glucose, however, yielded $[GLU]_{cyto}$ depletion under both conditions (Figure 5A). These results emphasize that the modulatory effect of K^+ on HKII activity requires the ability of HKII to associate with the outer mitochondrial membrane.

HKII remains mitochondria associated upon lowering $[K^+]_i$

Along these lines, we investigated whether low $[K^+]_i$ causes the inhibitory effect on HKII by affecting its mitochondrial association. Therefore, we expressed HKI-mRuby3 (Figure S4K) and HKII-EGFP (Figure S4N)

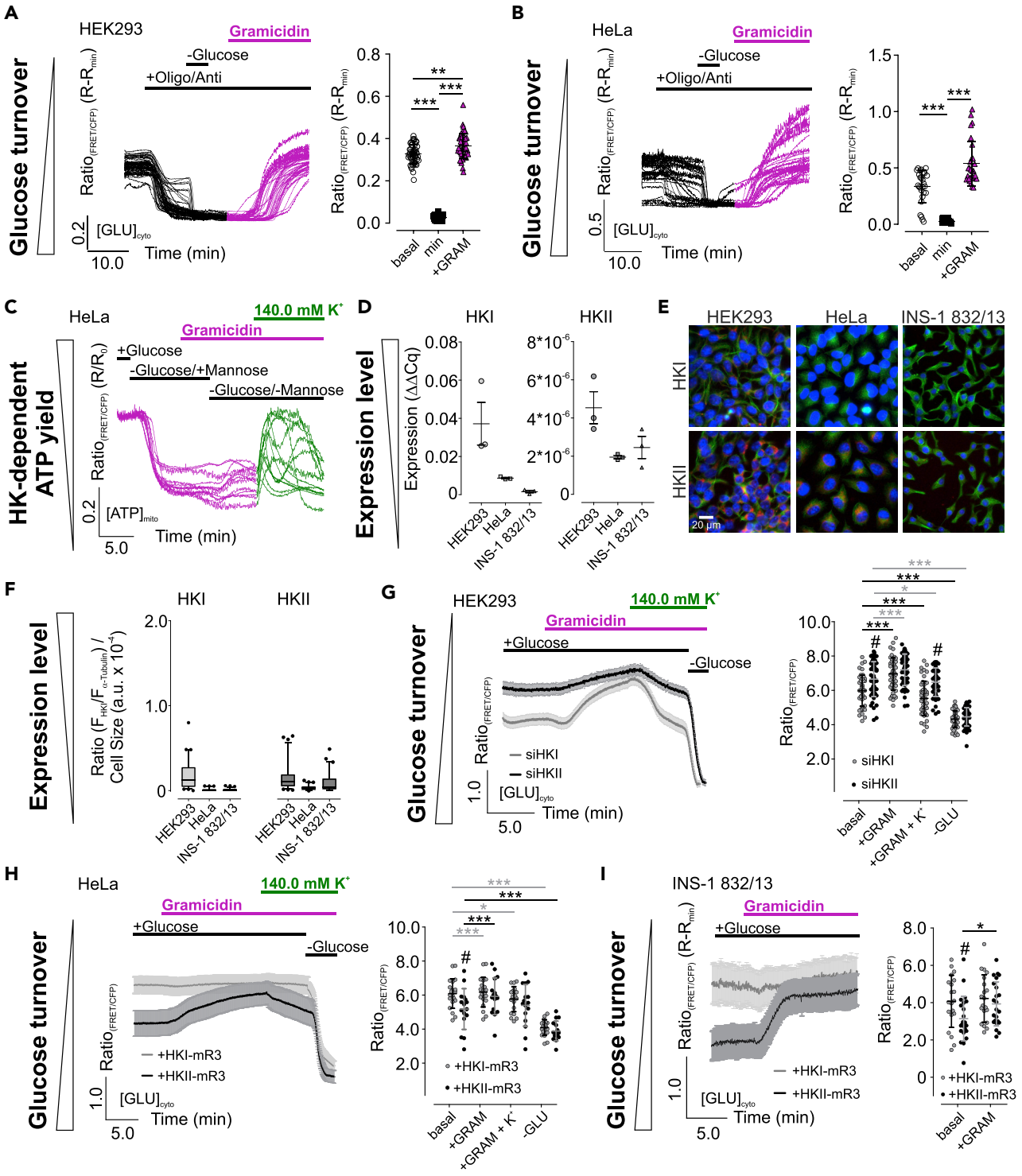

Figure 4. HKII status determines K^+ sensitivity of cell metabolism.

(A and B) $[GLU]_{cyto}$ over-time (left) and statistics (right) of HEK293 (A) and HeLa cells (B) in response to oligomycin-A and antimycin-A, glucose removal, or gramicidin treatment as indicated. Single cell responses and average ± standard deviation (SD) are shown. **p ≤ 0.01, ***p ≤ 0.001, Friedman test followed by Dunn's MC test. n = 3 for HEK293, n = 6 for HeLa.

(C) $[ATP]_{mito}$ dynamics of HeLa cells in response to gramicidin, mannose, and high $[K^+]_{ex}$. n = 4.

(D) Quantification of HKI (left) and HKII expression (right) in HEK293, HeLa, and INS-1 832/13 cells using quantitative PCR. Data represent each replicate and average ± standard error of mean. n = 3.

Figure 4. *Continued*

(E) Representative IF images of different cell lines. HKI or HKII (magenta), Hoechst (blue), and α-tubulin (green) are shown. Scale bar in the lower left image represents 10 μm. n ≥ 6.

(F) Quantification of HKI (left) and HKII expression (right) from images as shown in (E). Whiskers extend to the 5-95 percentile. Outliers are indicated as black dots. n ≥ 6.

(G–I) Average $[GLU]_{cyto}$ over-time ± standard error of mean (left) and corresponding statistics ± SD of HEK293 cells treated with siRNA against HKI (siHKI, light grey) or HKII (siHKII, black) (F), or HeLa (G), and INS-1 832/13 cells (H) either expressing HKI-mRuby3 (+HKI-mR3, light grey) or HKII-mRuby3 (+HKII-mR3, black), respectively. n ≥ 4. *p ≤ 0.05, ***p ≤ 0.001, Repeated measures one-way analysis of variance (ANOVA) test with Tukey's MC test (G, H), # and *p ≤ 0.05, Unpaired t test.

See also Figure S4.

simultaneously in HeLa cells. While both HK-FP fusion constructs (Figures S4K and S4N) remained mitochondria associated over-time under control conditions (Figures 5B and 5C), inhibition of HKII via 3-BP induced translocation of HKII-EGFP from the outer mitochondrial membrane (Figures 5B and 5C). We next depleted $[K^+]_i$, which did not affect HKI/II-FP localization ratio (Figures 5B and 5C). These results were furthermore confirmed by analyzing endogenous HKI and HKII localization by immunofluorescence. While the localization of HKI in HeLa cells did neither alter upon the administration of 3-BP nor upon treatment with gramicidin (Figures 5D and S4O), we found a reduced mitochondrial association of HKII upon 3-BP treatment (Figures 5E and S4P). Localization of HKII was, however, not affected upon depleting $[K^+]_i$ (Figures 5E and S4P). These data emphasize that low $[K^+]_i$ do not modulate HKII activity via inducing its translocation from mitochondria. Rather, K^+ has a direct effect on the catalytic activity of mitochondria-associated HKII in its physiologic environment.

Expression and activation of K_V1.3 abates glucose metabolism in HEK293 cells

Our findings imply that the presence and activity of specific K^+ channels in the plasma membrane (PM) should modulate HKII-dependent metabolism. To test this assumption, we expressed RFP-tagged K_V1.3 variants in HEK293 cells (Figures 6A and S5A). Patch-clamp experiments unveiled the functionality of TagRFP-K_V1.3, while TagRFP-K_V1.3 PD, possessing the single point mutation W388F (Figure S5A), showed less conductance (Figures 6B and S5B). A large portion of TagRFP-K_V1.3 was, however, found within intracellular structures (Figure S5C). Notably, the abundance of TagRFP-K_V1.3 at the PM was improved by unspecific K^+ channel inhibition using tetraethylammonium chloride (TEA), while the subcellular localization of TagRFP-Kv1.3 PD remained unchanged under these conditions (Figure S5C). TEA removal increased the K^+ currents of TagRFP-K_V1.3 across the PM (Figure S5D), drastically reduced $[K^+]_{cyto}$ (Figures 6C and 6D), and yielded $[GLU]_{cyto}$ accumulation (Figure 6E), indicative for a reduced glucose turnover upon K^+ efflux via TagRFP-K_V1.3. These signals were less pronounced in cells expressing TagRFP-K_V1.3 PD (Figures 6C and 6E). Under these conditions, $[K^+]_i$ and $[GLU]_{cyto}$ were restored upon administration of 30.0 mM K^+ to the extracellular space (Figures 6C and 6E). We furthermore analyzed the ECAR/OCR ratio of HEK293 cells stably expressing these K_V1.3 variants (Figure S5E). In the presence of PAP-1, a specific inhibitor of K_V1.3 (Schmitz et al., 2005) (Figure 6F), increased ECAR/OCR ratios of HEK293 cells stably expressing TagRFP-K_V1.3 were recorded (Figures 6G and S5F), emphasizing a promoted glycolytic activity by inhibition of cellular K^+ efflux. In contrast, PAP-1 neither affected ECAR nor OCR levels in HEK293 cells expressing TagRFP-K_V1.3 PD (Figure S5G). These data emphasize that the presence of specific K^+ channels, e.g. K_V1.3, may modulate cellular metabolic activity, especially of HKII-positive cells, and are in line with a recent report, demonstrating an implication of K_V1.3 inhibition on obesity and insulin resistance (Upadhyay et al., 2013).

DISCUSSION

Within this study, we visualized in single cells how $[K^+]_i$ fluctuations tightly and promptly affect intracellular levels of glucose, lactate, and ATP most likely as a consequence of controlling HKII-dependent cell metabolism primarily. By exploiting the first genetically encoded fluorescent biosensors for imaging $[K^+]_i$ in intact cells (Bischof et al., 2017), we established and tested protocols for efficient manipulation of $[K^+]_i$ using gramicidin, a well-characterized ionophoretic antibiotic peptide (Szule and Rand, 2003). Based on these protocols, we could correlate cellular K^+ depletion and restorations with subcellular metabolic and AMPK activities, demonstrating that only in cells with high HKII expression, K^+ is mandatory to maintain high aerobic glycolysis activities.

Our finding may especially gain importance in cancer biology due to the high expression of HKII in many cancer cells (Mathupala et al., 2006; Patra et al., 2013), particularly of those in tumors with bad prognosis (Anderson et al., 2017; Gong et al., 2012; Ogawa et al., 2015). In the light of several studies that point to

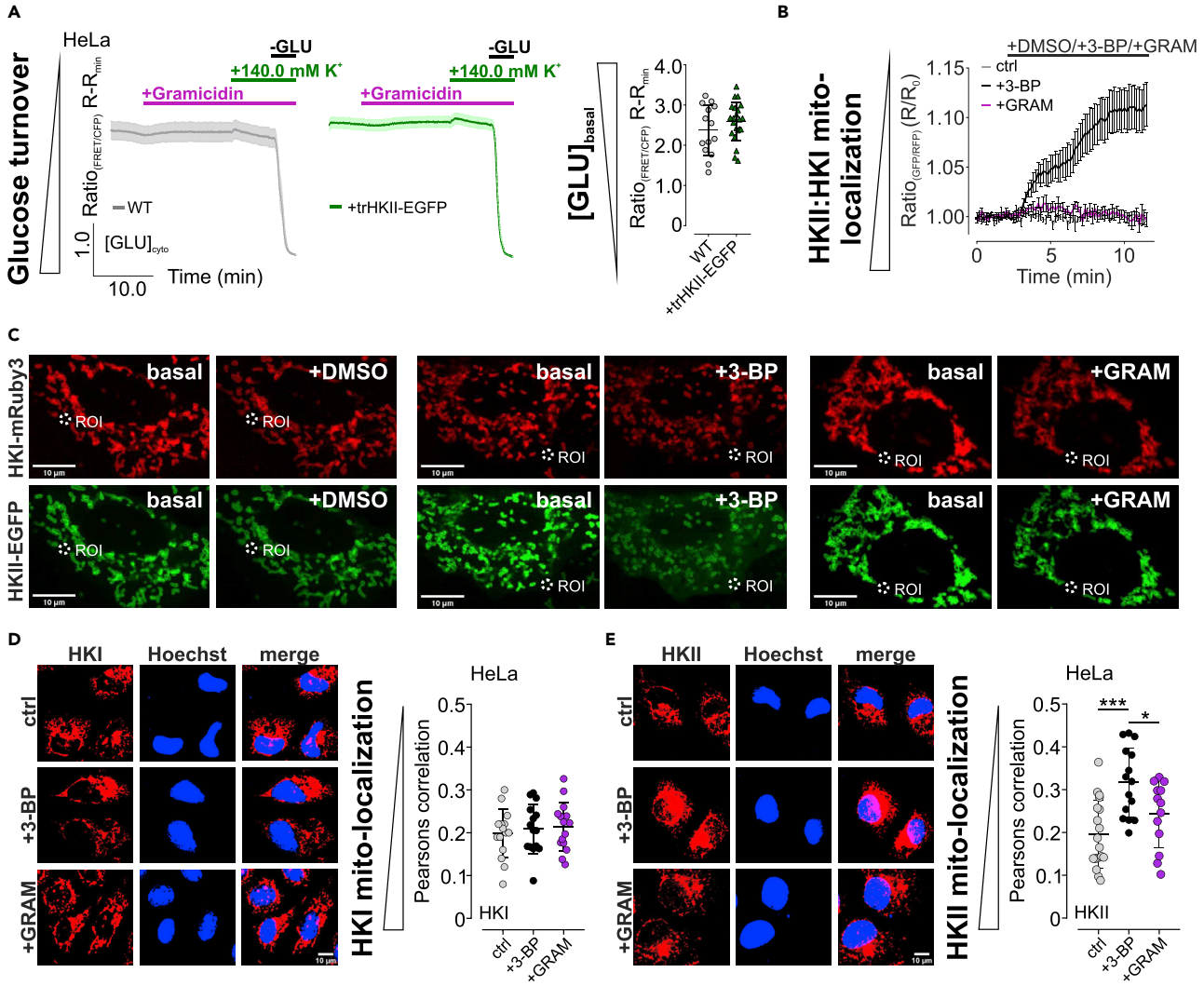

Figure 5. HKII remains mitochondria associated upon $[K^+]_i$ depletion and its mitochondrial association is required for the K^+-sensitive activity.

(A) $[GLU]_{cyto}$ over-time of HeLa WT cells (left panel, grey curve) or HeLa cells expressing trHKII-EGFP (middle panel, green curve) in response to gramicidin treatment in the absence of $[K^+]_{ex}$, upon $[K^+]_{ex}$ re-addition and upon glucose removal. Data show average ± standard error of mean, n = 4 for both conditions. Right panel demonstrates corresponding statistics, representing the basal FRET-ratio signal of FLII^{12}Pglu-700µδ6 expressed in HeLa WT cells or HeLa cells expressing trHKII-EGFP. n = 4 for both, data show each single cell and average ±standard deviation (SD).

(B and C) array confocal laser scanning microscope (ACLSM) images (C) and cytosolic fluorescence intensity ratios ± standard error of mean over-time (B) of regions of interest as demonstrated in (C). HeLa cells expressing HKI-mRuby3 (red, upper images) and HKII-EGFP (green, lower images) prior and after stimulation with DMSO (left), 3-BP (middle), or gramicidin (right) are shown. Scale bars show 10 µm. n ≥ 4 independent experiments for each condition.

(D) Left panel displays representative thresholded immunofluorescence images of HeLa cells stained for endogenous HKI (red, left panel, left images) and Hoechst for nuclear staining (blue, left panel, middle images). Right images demonstrate an overlay of HKI (red) and Hoechst staining (blue). HeLa cells were either untreated (ctrl, upper images) or treated with 3-BP (3-BP, middle images) or gramicidin (+GRAM) prior to fixation. Right panel represents corresponding statistics as Pearson correlation of HKI and Hoechst colocalization of every image acquired and mean ± SD of n = 3 independent experiments for each condition. Scale bar in the lower right image represents 10 µm.

(E) Left panel displays representative thresholded immunofluorescence images of HeLa cells stained for endogenous HKII (red, left panel, left images) and Hoechst for nuclear staining (blue, left panel, middle images). Right images demonstrate an overlay of HKII (red) and Hoechst staining (blue). HeLa cells were either untreated (ctrl, upper images) or treated with 3-BP (3-BP, middle images) or gramicidin (+GRAM) prior to fixation. Right panel represents corresponding statistics as Pearson correlation of HKII and Hoechst colocalization of every image acquired and mean ± SD of n = 3 independent experiments for each condition. *p ≤ 0.05, ***p ≤ 0.001, one-way ANOVA test with Tukey's MC test. Scale bar in the lower right image represents 10 µm. See also Figure S4.

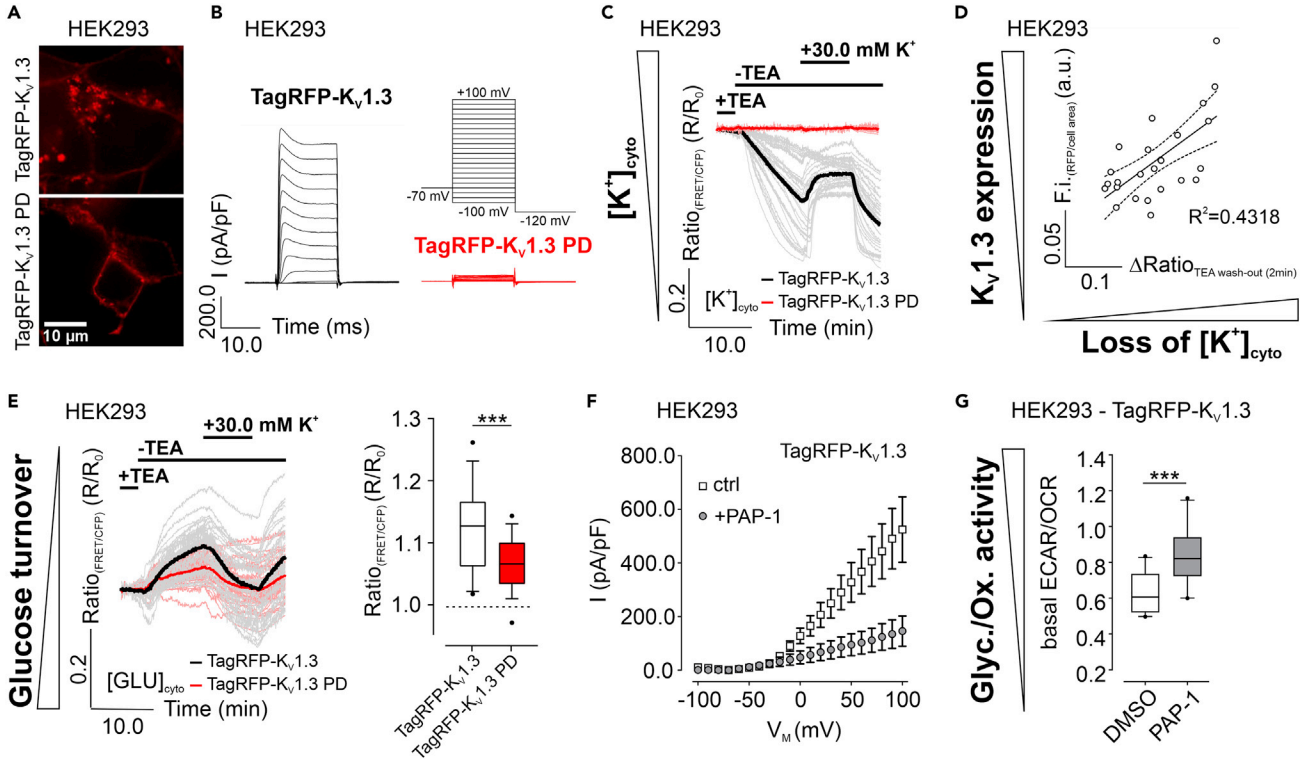

Figure 6. Consequences of voltage-gated K^+ channel expression on metabolism.

(A and B) Representative ACLSM images (A) and currents (B) of HEK293 cells either expressing TagRFP-K_V1.3 (upper image and black traces) or TagRFP-K_V1.3 PD (lower image and red traces). Scale bar shows 10 µm. n ≥ 12.

(C and E) (C) Average (bold) and single cell (faint) $[K^+]_{cyto}$ and (E) $[GLU]_{cyto}$ over-time of HEK293 cells either expressing TagRFP-K_V1.3 (black) or TagRFP-K_V1.3 PD (red). At the time point indicated, TEA was removed, followed by a re-addition of 30.0 mM K^+. n ≥ 3.

(D) Correlation of $[K^+]_{cyto}$ loss with TagRFP-K_V1.3 expression in HEK293 cells. n = 3.

(F) IV curves ± standard error of mean of HEK293 cells stably expressing TagRFP-K_V1.3, either in the absence (ctrl, white) or presence of 1 µM PAP-1 (+PAP-1, grey). n ≥ 13.

(G) Basal ECAR/OCR ratios of HEK293 cells expressing TagRFP-K_V1.3, either in the presence of DMSO (white) or PAP-1 (grey). Whiskers extend to the 5-95 percentile. Outliers are indicated as black dots. n = 3, ***p ≤ 0.001, Unpaired t test.

See also Figure S5.

K^+ channels and the cellular K^+ homeostasis as important determinants of tumorigenesis, tumor progression, and tumor malignancy (Lansu and Gentile, 2013; Mohr et al., 2019, 2020; Steudel et al., 2017; Urrego et al., 2014), our study linking $[K]_i$ to tumor cell metabolism is particularly interesting as it has the potency to lead to the development of novel anticancer strategies. Importantly, while we here provide different EC_{50} values ranging from 3 mM to 70 mM for $[K^+]_i$ to alter $[GLU]_{cyto}$ and $[ATP]_{mito}$ in HKII-expressing single cells, our study is less conclusive if unphysiological strong or already moderate physiological $[K^+]_i$ fluctuations significantly modulate cell metabolism and thus the proliferation rates of HKII-expressing cells. However, it is tempting to speculate that buffering extracellular K^+ specifically within the tumor microenvironment, in which $[K^+]_{ex}$ compared to healthy tissues is significantly increased (Eil et al., 2016), might attenuate the metabolic activity of HKII-positive tumor cells. Notably, here we could demonstrate that the same voltage-gated K^+ channel, K_V1.3, which rescued T cells from high $[K^+]_{ex}$-mediated immune suppression (Eil et al., 2016), affected $[K^+]_i$ and consequently controlled $[GLU]_{cyto}$ most likely by regulating HKII activity. Much more research is essential to further validate if this finding can be exploited therapeutically. However, we here highlight that the heterologous expression of voltage-gated K^+ channel associates with metabolic alterations. Nonetheless, such an approach would require a high cancer cell specificity without severely affecting the function of other tissues or organs, as HKII is also found in insulin-sensitive tissues, muscle cells, or adipocytes (Mathupala et al., 2006; Roberts and Miyamoto, 2015; Wilson, 2003). Also, in these aspects, our study asks for further research to investigate whether global or local K^+ fluctuations control the metabolic activity of single cells, organs, or even whole animals, as K^+ might represent an essential regulatory component of mitochondria-associated HKII.

Our results strongly emphasize that $[K^+]_i$ acts as an important and direct modulator of HKII activity in multiple cell lines, independent of their origin. However, additional research needs to be conducted to identify the K^+-sensitive structures of the enzyme and to understand the exact molecular mechanism by which K^+ might control the enzymatic activity. Our predictions of several positions within a model of HKII that may directly bind K^+ might be helpful in this context. However, it remains unclear if the thermal inactivation of HKII *in vitro*, which is under the control of K^+ (Nawaz et al., 2018), is based on the same or similar mechanisms as the loss of HKII activity in K^+-depleted cells. In this context, it would be also important to understand if K^+ might alter the inhibitory effect of glucose-6-phosphate, i.e. the product inhibition of HKII. Our experiments exclude that low K^+ affects the mitochondrial localization of HKII, which is based on the N-terminus of the enzyme and facilitates ATP supply to the enzyme (Sun et al., 2008). However, by exploiting a truncated version of HKII, which is unable to localize to mitochondria, we show evidence that the localization of HKII to mitochondria is essential to control glycolysis and ATP generation by $[K^+]_i$. Thus, it is tempting to speculate that not only global, but also particularly local subcellular K^+ signals on the surface of mitochondria might regulate cell metabolism in subdomains of a cell by controlling the activity of HKII. Such microdomains might, for example, be formed at the close vicinity to VDAC due to its cation gating function, consequently impacting on the activity of VDAC-associated HKII (Pastorino and Hoek, 2008). Following this study, targeted fluorescent biosensors (Bischof et al., 2017; Burgstaller et al., 2019; Imamura et al., 2009; Takanaga et al., 2008), informative protocols, and experimental settings including *in vivo* animal models might help to identify and unravel local K^+-dependent metabolic settings in health and disease.

Limitations of the study

Our data were generated in well-established cell lines. Hence, whether and how cellular K^+ fluctuations and $[K^+]_i$ alterations modulate HKII activity in isolated primary cells or even living animals remains elusive and will be part of future studies. Moreover, our study does not address whether increases of $[K^+]_{ex}$, as found within the tumor microenvironment, promote tumor cell proliferation by stimulating HKII-dependent glycolysis and if the manipulation of $[K^+]_i$ and/or $[K^+]_{ex}$ represents a feasible therapeutic strategy to fight cancers by altering their metabolic activity.

Resource availability

Lead contact

Further information and requests for resources and reagents should be directed to and will be fulfilled by the lead contact, Helmut Bischof (helmut.bischof@uni-tuebingen.de).

Materials availability

Plasmids generated in this study are available from the lead contact upon request.

Data and code availability

Original/source data for all figures in the paper are available from the lead contact upon request.

METHODS

All methods can be found in the accompanying transparent methods supplemental file.

SUPPLEMENTAL INFORMATION

Supplemental information can be found online at https://doi.org/10.1016/j.isci.2021.102346.

ACKNOWLEDGMENTS

We thank C.B. Newgard, Department of Pharmacology and Cancer Biology, Duke University School of Medicine, USA, for INS-1 832/13 cells. This work was funded by the Alexander von Humboldt Foundation (H.B.), the Austrian Infrastructure Program 2016/2017 (T.M.), the Austrian Research Promotion Agency (FFG), project numbers 864690 and 870454 (T.M.), the Austrian Science Fund *(FWF)*, project numbers I3716 (R.M.), P3326 (K.G.), P28701 (R.S.), P28854 and I3792 (T.M.), and W1226 (T.M., W.F.G.), BioTechMed Graz (Flagship project) (T.M.), the Brain & Behavior Research Foundation NARSAD Young Investigator Grant 20748 (L.M.), the German Research Foundation (DFG), project numbers RL 1490/10-1 (R.L.), MA 8113/2-1 (L.M.), and DFG PL 249 15-1 (N.P.), the Germany's Excellence Strategy within the framework of the Munich Cluster for Systems Neurology (EXC 2145 SyNergy – ID 390857198) (N.P.), the ICEPHA Graduate

Program "Membrane-associated Drug Targets in Personalized Cancer Medicine" (R.L.), the Integrative Metabolism Research Center Graz (T.M.), the Styrian Government (Zukunftsfond) (T.M.), and the Wilhelm Schuler Stiftung (L.M.). T.R. and T.S. are doctoral fellows (Molecular Medicine, Medical University of Graz). O.A.B. is a doctoral fellow of the doctoral program Metabolic and Cardiovascular Disease (MCD).

AUTHOR CONTRIBUTIONS

H.B., R.L., W.F.G., and R.M., were involved in conceptualization; H.B., S.B., A.S., L.M., and T.S. were involved in data curation; H.B., S.B., A.S., L.M., O.A.B., and T.M. assisted in formal analysis; H.B., K.G., R.S., T.M., N.P., R.L., W.F.G., and R.M. acquired financial support; H.B., S.B., A.S., L.M., and T.S. were involved in investigations; H.B., S.B., R.S., T.M., R.L., and R.M. designed the methodology; H.B., R.L., W.F.G., and R.M. performed project administration; L.M., K.G., R.S., T.M., N.P., R.L., W.F.G., and R.M. provided resources; R.L., W.F.G., and R.M. supervised the project, H.B. and S.B. visualized data, H.B., R.L., W.F.G., and R.M. wrote the original draft. All authors critically reviewed the manuscript and stated comments.

DECLARATION OF INTERESTS

The authors declare no competing interests.

Received: December 15, 2020
Revised: February 22, 2021
Accepted: March 18, 2021
Published: April 23, 2021

REFERENCES

Abu-Hamad, S., Zaid, H., Israelson, A., Nahon, E., and Shoshan-Barmatz, V. (2008). Hexokinase-I protection against apoptotic cell death is mediated via interaction with the voltage-dependent anion channel-1. J. Biol. Chem. *283*, 13482–13490.

Anderson, M., Marayati, R., Moffitt, R., and Yeh, J.J. (2017). Hexokinase 2 promotes tumor growth and metastasis by regulating lactate production in pancreatic cancer. Oncotarget *8*, 56081–56094.

Bermejo, C., Haerizadeh, F., Takanaga, H., Chermak, D., and Frommer, W.B. (2010). Dynamic analysis of cytosolic glucose and ATP levels in yeast using optical sensors. Biochem. J. *432*, 399–406.

Bischof, H., Rehberg, M., Stryeck, S., Artinger, K., Eroglu, E., Waldeck-Weiermair, M., Gottschalk, B., Rost, R., Deak, A.T., Niedrist, T., et al. (2017). Novel genetically encoded fluorescent probes enable real-time detection of potassium in vitro and in vivo. Nat. Commun. *8*, 1422.

Bischof, H., Burgstaller, S., Waldeck-Weiermair, M., Rauter, T., Schinagl, M., Ramadani-Muja, J., Graier, W.F., and Malli, R. (2019). Live-cell imaging of physiologically relevant metal ions using genetically encoded FRET-based probes. Cells *8*, 492.

Burgstaller, S., Bischof, H., Gensch, T., Stryeck, S., Gottschalk, B., Ramadani-Muja, J., Eroglu, E., Rost, R., Balfanz, S., Baumann, A., et al. (2019). pH-lemon, a fluorescent protein-based pH reporter for acidic compartments. ACS Sens. *4*, 883–891.

Depaoli, M.R., Karsten, F., Madreiter-Sokolowski, C.T., Klec, C., Gottschalk, B., Bischof, H., Eroglu, E., Waldeck-Weiermair, M., Simmen, T., Graier, W.F., et al. (2018). Real-time imaging of mitochondrial ATP dynamics reveals the metabolic setting of single cells. Cell Rep. *25*, 501–512.e3.

Eil, R., Vodnala, S.K., Clever, D., Klebanoff, C.A., Sukumar, M., Pan, J.H., Palmer, D.C., Gros, A., Yamamoto, T.N., Patel, S.J., et al. (2016). Ionic immune suppression within the tumour microenvironment limits T cell effector function. Nature *537*, 539–543.

Gong, L., Cui, Z., Chen, P., Han, H., Peng, J., and Leng, X. (2012). Reduced survival of patients with hepatocellular carcinoma expressing hexokinase II. Med. Oncol. *29*, 909–914.

Gottlob, K. (2001). Inhibition of early apoptotic events by Akt/PKB is dependent on the first committed step of glycolysis and mitochondrial hexokinase. Genes Dev. *15*, 1406–1418.

Guerrero, A., Herranz, N., Sun, B., Wagner, V., Gallage, S., Guiho, R., Wolter, K., Pombo, J., Irvine, E.E., Innes, A.J., et al. (2019). Cardiac glycosides are broad-spectrum senolytics. Nat. Metab. *1*, 1074–1088.

Hardie, D.G., Ross, F.A., and Hawley, S.A. (2012). AMPK: a nutrient and energy sensor that maintains energy homeostasis. Nat. Rev. Mol. Cell Biol. *13*, 251–262.

Heaton, A.L., and Armentrout, P.B. (2008). Experimental and theoretical studies of potassium cation interactions with the acidic amino acids and their amide derivatives. J. Phys. Chem. B *112*, 12056–12065.

Huang, X., and Jan, L.Y. (2014). Targeting potassium channels in cancer. J. Cell Biol. *206*, 151–162.

Imamura, H., Huynh Nhat, K.P., Togawa, H., Saito, K., Iino, R., Kato-Yamada, Y., Nagai, T., and Noji, H. (2009). Visualization of ATP levels inside single living cells with fluorescence resonance energy transfer-based genetically encoded indicators. PNAS *106*, 15651–15656.

Lansu, K., and Gentile, S. (2013). Potassium channel activation inhibits proliferation of breast cancer cells by activating a senescence program. Cell Death Dis. *4*, e652.

Mathupala, S.P., Ko, Y.H., and Pedersen, P.L. (2006). Hexokinase II: cancer's double-edged sword acting as both facilitator and gatekeeper of malignancy when bound to mitochondria. Oncogene *25*, 4777–4786.

Mathupala, S.P., Ko, Y.H., and Pedersen, P.L. (2009). Hexokinase-2 bound to mitochondria: cancer's stygian link to the "Warburg effect" and a pivotal target for effective therapy. Semin. Cancer Biol. *19*, 17–24.

Mohr, C.J., Gross, D., Sezgin, E.C., Steudel, F.A., Ruth, P., Huber, S.M., and Lukowski, R. (2019). $K_{Ca}3.1$ channels confer radioresistance to breast cancer cells. Cancers (Basel) *11*, 1285.

Mohr, C.J., Schroth, W., Mürdter, T.E., Gross, D., Maier, S., Stegen, B., Dragoi, A., Steudel, F.A., Stehling, S., Hoppe, R., et al. (2020). Subunits of BK channels promote breast cancer development and modulate responses to endocrine treatment in preclinical models. Br. J. Pharmacol. https://doi.org/10.1111/bph.15147.

Najafov, A., Luu, H.S., Mookhtiar, A.K., Mifflin, L., Xia, H., Amin, P.P., Ordureau, A., Wang, H., and Yuan, J. (2020). RIPK1 promotes energy sensing by the mTORC1 pathway. Mol. Cell *81*, 370–385.e7.

Nawaz, M.H., Ferreira, J.C., Nedyalkova, L., Zhu, H., Carrasco-López, C., Kirmizialtin, S., and

Rabeh, W.M. (2018). The catalytic inactivation of the N-half of human hexokinase 2 and structural and biochemical characterization of its mitochondrial conformation. Biosci. Rep. *38*, BSR20171666.

Ogawa, H., Nagano, H., Konno, M., Eguchi, H., Koseki, J., Kawamoto, K., Nishida, N., Colvin, H., Tomokuni, A., Tomimaru, Y., et al. (2015). The combination of the expression of hexokinase 2 and pyruvate kinase M2 is a prognostic marker in patients with pancreatic cancer. Mol. Clin. Oncol. *3*, 563–571.

Palmer, B.F. (2015). Regulation of potassium homeostasis. CJASN *10*, 1050–1060.

Pastorino, J.G., and Hoek, J.B. (2008). Regulation of hexokinase binding to VDAC. J. Bioenerg. Biomembr. *40*, 171–182.

Patra, K.C., Wang, Q., Bhaskar, P.T., Miller, L., Wang, Z., Wheaton, W., Chandel, N., Laakso, M., Muller, W.J., Allen, E.L., et al. (2013). Hexokinase 2 is required for tumor initiation and maintenance and its systemic deletion is therapeutic in mouse models of cancer. Cancer Cell *24*, 213–228.

Peng, S.-Y., Lai, P.-L., Pan, H.-W., Hsiao, L.-P., and Hsu, H.-C. (2008). Aberrant expression of the glycolytic enzymes aldolase B and type II hexokinase in hepatocellular carcinoma are predictive markers for advanced stage, early recurrence and poor prognosis. Oncol. Rep. *19*, 1045–1053.

Roberts, D.J., and Miyamoto, S. (2015). Hexokinase II integrates energy metabolism and cellular protection: akting on mitochondria and TORCing to autophagy. Cell Death Differ. *22*, 248–257.

Rosano, C., Sabini, E., Rizzi, M., Deriu, D., Murshudov, G., Bianchi, M., Serafini, G., Magnani, M., and Bolognesi, M. (1999). Binding of non-catalytic ATP to human hexokinase I highlights the structural components for enzyme–membrane association control. Structure *7*, 1427–1437.

Rose, I.A., and Warms, J.V.B. (1982). Stability of hexokinase II in Vitro and in ascites tumor cells. Arch. Biochem. Biophys. *213*, 625–634.

San Martín, A., Ceballo, S., Ruminot, I., Lerchundi, R., Frommer, W.B., and Barros, L.F. (2013). A genetically encoded FRET lactate sensor and its use to detect the Warburg effect in single cancer cells. PLoS One *8*, e57712.

Sanderson, S.M., Xiao, Z., Wisdom, A.J., Bose, S., Liberti, M.V., Reid, M.A., Hocke, E., Gregory, S.G., Kirsch, D.G., and Locasale, J.W. (2020). The Na^+/K^+ ATPase Regulates Glycolysis and Modifies Immune Metabolism in Tumors (Cancer Biology).

Schmitz, A., Sankaranarayanan, A., Azam, P., Schmidt-Lassen, K., Homerick, D., Hänsel, W., and Wulff, H. (2005). Design of PAP-1, a selective small molecule Kv1.3 blocker, for the suppression of effector memory T cells in autoimmune diseases. Mol. Pharmacol. *68*, 1254–1270.

Steudel, F.A., Mohr, C.J., Stegen, B., Nguyen, H.Y., Barnert, A., Steinle, M., Beer-Hammer, S., Koch, P., Lo, W.-Y., Schroth, W., et al. (2017). SK4 channels modulate Ca^{2+} signalling and cell cycle progression in murine breast cancer. Mol. Oncol. *11*, 1172–1188.

Sun, L., Shukair, S., Naik, T.J., Moazed, F., and Ardehali, H. (2008). Glucose phosphorylation and mitochondrial binding are required for the protective effects of hexokinases I and II. MCB *28*, 1007–1017.

Szule, J.A., and Rand, R.P. (2003). The effects of gramicidin on the structure of phospholipid assemblies. Biophys. J. *85*, 1702–1712.

Takanaga, H., Chaudhuri, B., and Frommer, W.B. (2008). GLUT1 and GLUT9 as major contributors to glucose influx in HepG2 cells identified by a high sensitivity intramolecular FRET glucose sensor. Biochim. Biophys. Acta *1778*, 1091–1099.

Triana-Martínez, F., Picallos-Rabina, P., Da Silva-Álvarez, S., Pietrocola, F., Llanos, S., Rodilla, V., Soprano, E., Pedrosa, P., Ferreirós, A., Barradas, M., et al. (2019). Identification and characterization of Cardiac Glycosides as senolytic compounds. Nat. Commun. *10*, 4731.

Tsou, P., Zheng, B., Hsu, C.-H., Sasaki, A.T., and Cantley, L.C. (2011). A fluorescent reporter of AMPK activity and cellular energy stress. Cell Metab. *13*, 476–486.

Upadhyay, S.K., Eckel-Mahan, K.L., Mirbolooki, M.R., Tjong, I., Griffey, S.M., Schmunk, G., Koehne, A., Halbout, B., Iadonato, S., Pedersen, B., et al. (2013). Selective Kv1.3 channel blocker as therapeutic for obesity and insulin resistance. Proc. Natl. Acad. Sci. *110*, E2239–E2248.

Urrego, D., Tomczak, A.P., Zahed, F., Stuhmer, W., and Pardo, L.A. (2014). Potassium channels in cell cycle and cell proliferation. Philos. Trans. R. Soc. B Biol. Sci. *369*, 20130094.

Wilson, J.E. (2003). Isozymes of mammalian hexokinase: structure, subcellular localization and metabolic function. J. Exp. Biol. *206*, 2049–2057.

iScience, Volume *24*

Supplemental information

Potassium ions promote hexokinase-II dependent glycolysis

Helmut Bischof, Sandra Burgstaller, Anna Springer, Lucas Matt, Thomas Rauter, Olaf A. Bachkönig, Tony Schmidt, Klaus Groschner, Rainer Schindl, Tobias Madl, Nikolaus Plesnila, Robert Lukowski, Wolfgang F. Graier, and Roland Malli

Supplementary Figures and Captions

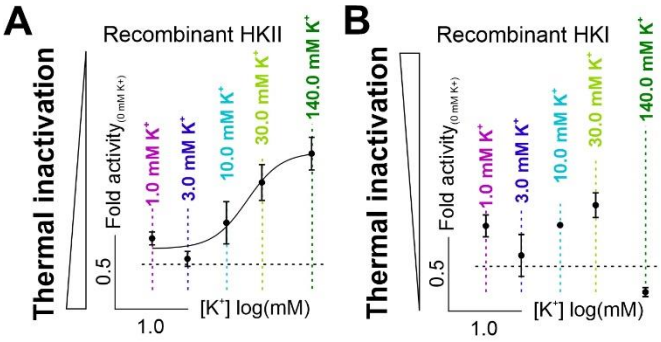

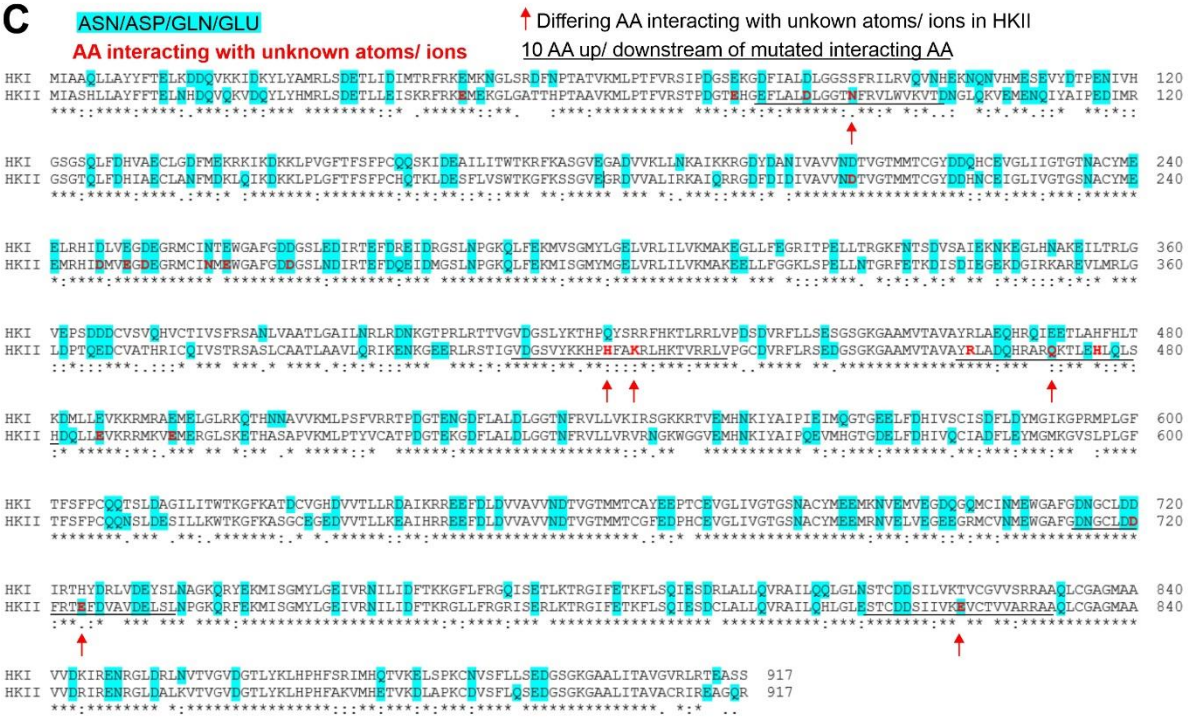

D

Interaction site	Amino acid position	Hexokinase I	Hexokinase II
1	46	E	E
	267	D	D
2	76	E	E
	462	R	R
3	84	D	D
	89	S	N
4	209	D	D
	258	N	N
5	235	N	N
	260	E	E
6	246	D	D
	249	E	E
	251	D	D
7	422	Q	H
	425	R	K
8	471	E	Q
	821	T	E
9	476	H	H
	724	H	E
10	486	E	E
	494	E	E
	720	D	D

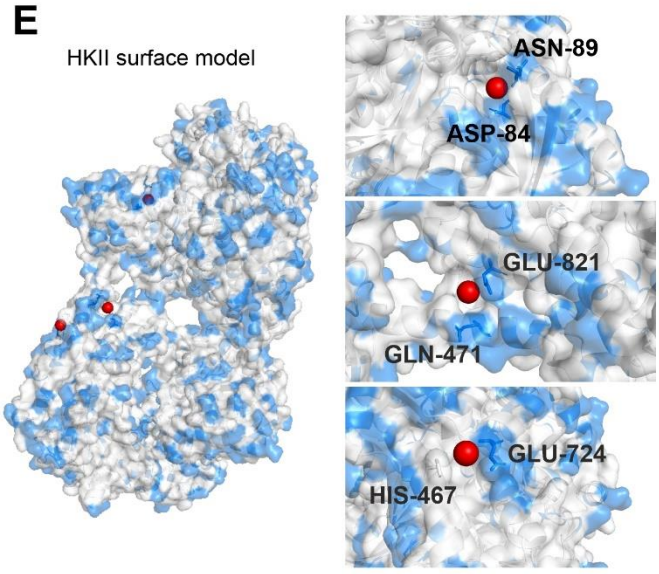

Figure S1. Properties of HKI and HKII, related to Figure 1. (**A, B**) Mean activity ± SEM of purified HKII (**A**) and HKI (**B**) after thermal inactivation at 37°C for 1.5 hours in the presence of different [K^+]. n=3 for both proteins and all [K^+]. (**B**) Protein sequence alignment of HKI vs. HKII. Potential K^+ binding

amino acids (ASN, ASP, GLN, GLU) are highlighted in blue, amino acids interacting with unknown ions or atoms in the crystal structure of HKII are written in red. Red arrows indicate a differing amino acid between HKI and HKII, which is interacting with an unknown atom or ion in HKII. Underlined regions highlight 10 amino acids up and downstream of such amino acid. (**D**) Overview of the 10 potential interaction sites as found in HKII. Interaction site (1-10), corresponding positions of the interacting amino acids and the respective amino acids found in HKI or HKII are indicated in one-letter code. Red background shows interaction sites that differ between HKI and HKII, amino acids written in red and bold highlight differing amino acids between HKI and HKII. (**E**) Surface model of HKII. Unknown atoms or ions close to the 3 interaction sites that possess a potential K^+ binding amino acid in HKII, but not HKI (**D**, interaction site 3, 8, 9) are shown in red.

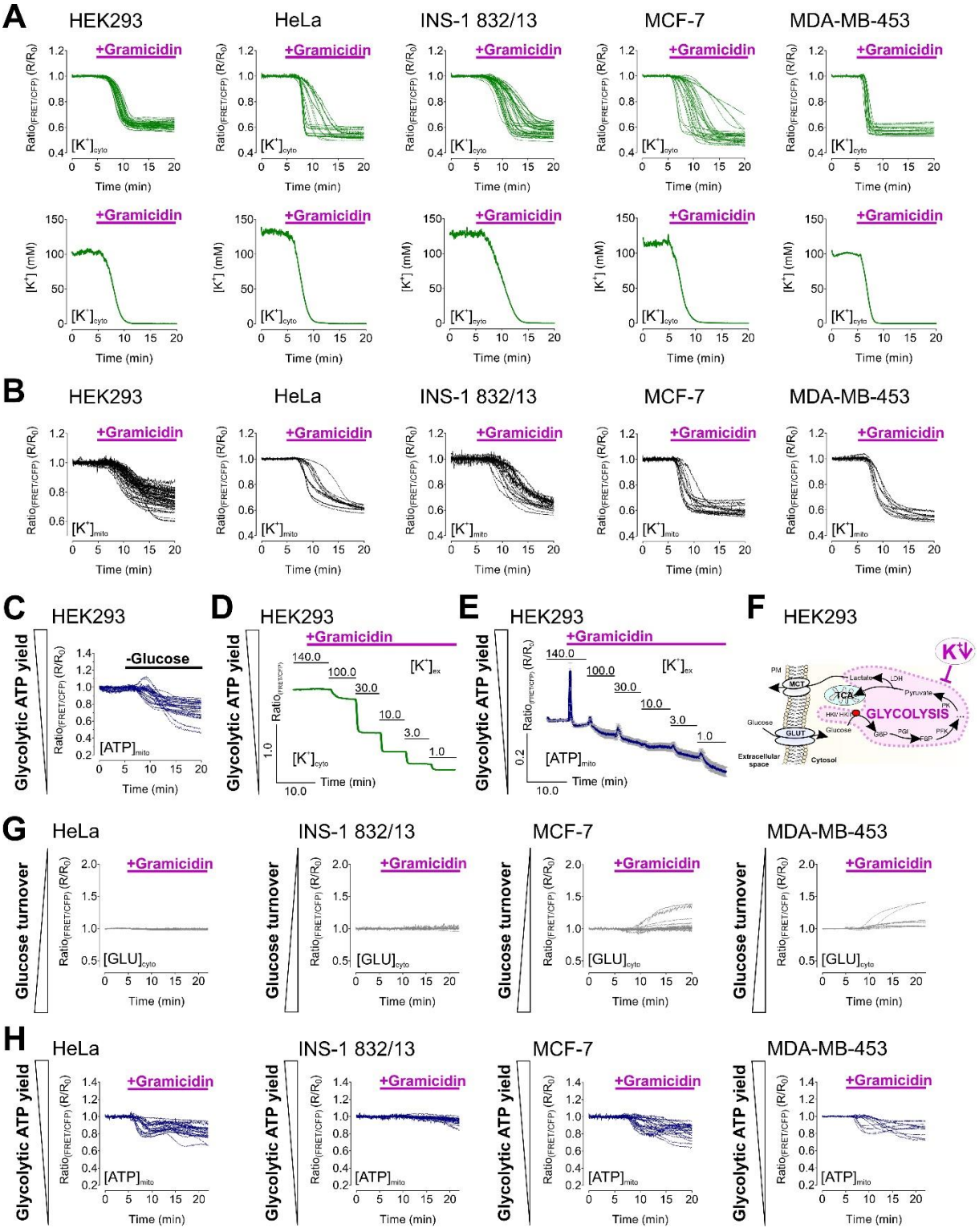

Figure S2. Intracellular K^+ depletion induces disturbances of cellular energy homeostasis, related to Figure 1 and Figure 2. (**A, B**) FRET-ratio signals over-time of HEK293 (first panel), HeLa (second panel), INS-1 832/13 (third panel), MCF-7 (fourth panel), and MDA-MB-453 cells (fifth panel), expressing NES lc-LysM GEPII 1.0 (**A**) or mt lc-LysM GEPII 1.0 (**B**), genetically encoded, FRET-based K^+ indicators targeted to the cytosol or the mitochondrial matrix, respectively. Lower row in (**A**) demonstrates representative $[K^+]_{cyto}$ of single cells over-time. At the time points indicated in the panels, 15 µM gramicidin were administered to the cells. Data demonstrate each single cell response. n=3 for all. (**C**) Single cell responses over-time of HEK293 cells expressing mtAT1.03 in response to the removal of extracellular glucose. n=4. (**D**) Representative single cell response of a HEK293 cell expressing NES lc-LysM GEPII 1.0 in response to treatment with gramicidin in the presence of decreasing $[K^+]_{ex}$ ranging from 140.0 mM – 1.0 mM as indicated in the panel. n=3. (**E**) $[ATP]_{mito}$ over-time of HEK293 cells in

response to gramicidin treatment, followed by decreasing $[K^+]_{ex}$ from 140.0 mM to 1.0 mM as indicated in the panel. Data shows average ± SEM of 3 independent experiments. (**F**) Schematic illustration of K^+ modulated metabolism. (**G, H**) FRET-ratio signals over-time of HeLa, INS-1 832/13, MCF-7 and MDA-MB-453 cells (from left to right) either expressing FLII^{12}Pglu-700µδ6 (**G**, grey curves) or mtAT1.03 (**H**, blue curves). At the time point indicated in the panels, 15 µM gramicidin were administered to the cells. Data demonstrate each single cell response. (**G**) n=3 for HeLa, n=4 for INS-1 832/13, n=4 for MCF-7 and n=4 for MDA-MB-453. (**H**) n=5 for HeLa, n=5 for INS-1 832/13, n=5 for MCF-7 and n=4 for MDA-MB-453.

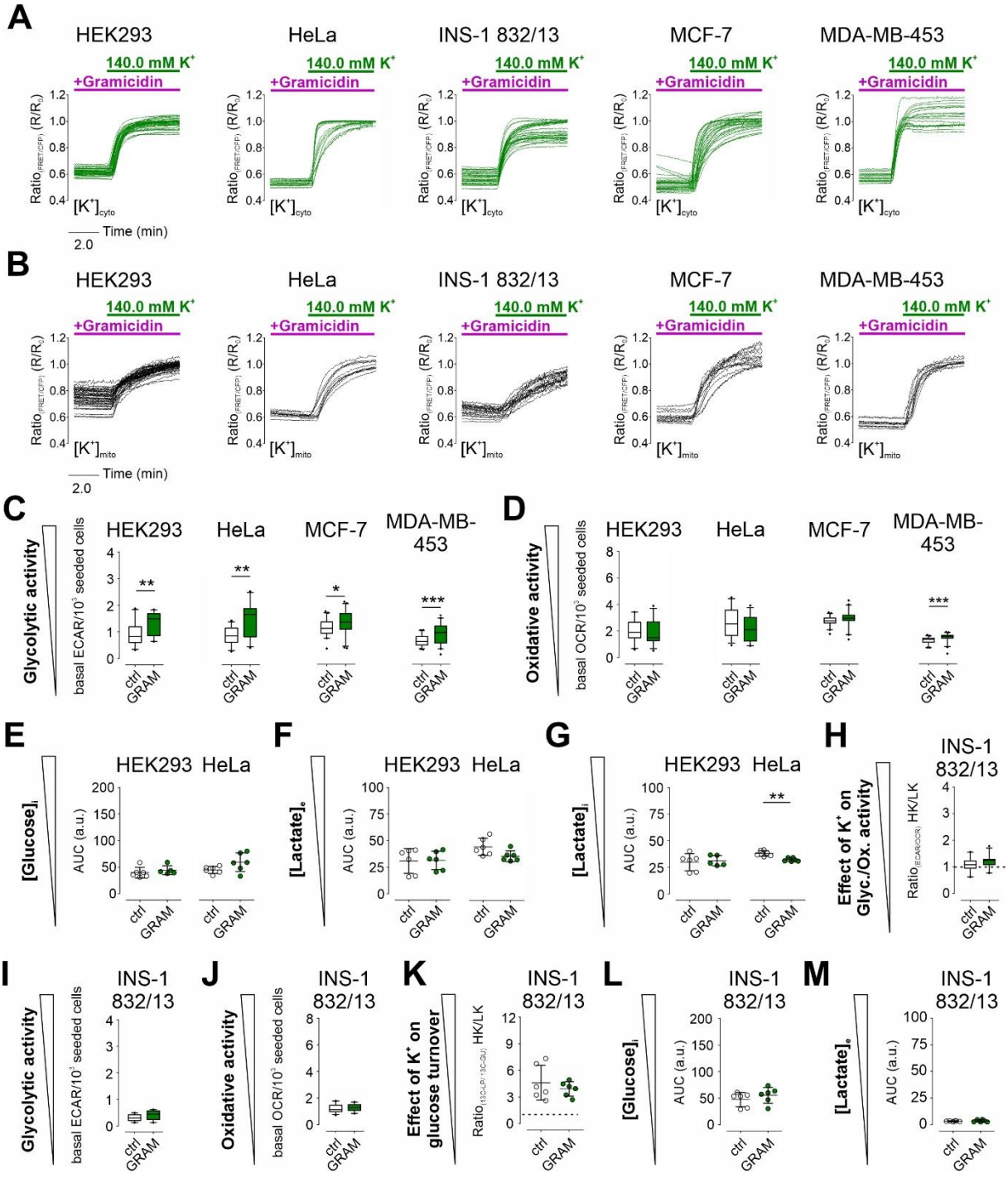

Figure S3. Restoring high $[K^+]_i$ restores aerobic glycolysis, related to Figure 3. (**A, B**) FRET-ratio signals over-time of different cell lines as indicated, expressing NES lc-LysM GEPII 1.0 (**A**) or mt lc-LysM GEPII 1.0 (**B**), genetically encoded, FRET-based K^+ indicators targeted to the cytosol or the mitochondrial matrix, respectively. Cells were treated with gramicidin in the absence of extracellular K^+, followed by the addition of 140.0 mM K^+ via a gravity-based perfusion system at time points indicated. n=3 for all. (**C, D**) Basal ECAR (**C**) and OCR (**D**) levels/10^3 seeded cells of (from left to right) HEK293, HeLa, MCF-7, and MDA-MB-453 cells. Cells were either treated with DMSO (ctrl, white boxes, all panels) or gramicidin (GRAM, green boxes, all panels). Boxes indicate the median and the first- and third quartile. Lower and upper whiskers indicate 5-95 percentile, outliers are indicated as black dots. n=4 for all. (**C**) *p≤0.05, **p≤0.01, ***p≤0.001 either using Unpaired t-test (HeLa and MCF-7) or Mann-Whitney test (HEK293, MDA-MB-453). (**D**) ***p≤0.001 using Mann-Whitney test. (**E-G**) Graphs show the area under the curve (AUC) of ^{13}C-labelled glucose in the cell lysate (**E**), AUC of ^{13}C-labelled lactate in the supernatant (**F**), or AUC of ^{13}C-labelled lactate in the cell lysate (**G**) of HEK293 (left, all panels) or HeLa (right, all panels). Cells were either treated with DMSO (ctrl, white circles, all panels) or gramicidin

(GRAM, green circles, all panels) in the presence of 140.0 mM K^+. Data represent each replicate and average ± SD. n=6 for all. **p=0.0022, Mann-Whitney test. (**H-J**) Basal 140.0 mM K^+ (HK)/0 mM K^+ (LK) ECAR/OCR ratios (**H**), basal ECAR levels/10^3 seeded cells (**I**) and basal OCR levels/10^3 seeded cells (**J**) of INS-1 832/13 cells either treated with DMSO (ctrl, white boxes) or gramicidin (GRAM, green boxes) in the presence of 140.0 mM K^+. n=4. Boxes indicate the median and the first- and third quartile. Lower and upper whiskers indicate 5-95 percentile, outliers are indicated as black dots. (**K**) 140.0 mM K^+ (HK)/0 mM K^+ (LK) ^{13}C-LP/^{13}C-GU ratios of INS-1 832/13 cells either treated with DMSO (ctrl, white circles) or gramicidin (GRAM, green circles). n=4. Data represents each replicate and average ± SD. (**L, M**) AUC of ^{13}C-labelled glucose in the cell lysate (**L**) and AUC of ^{13}C-labelled lactate in the supernatant (**M**) of INS-1 832/13 cells. Cells were either treated with DMSO (ctrl, white circles, both panels) or gramicidin (GRAM, green circles, both panels) in the presence of 140.0 mM K^+. Data shows each replicate and average ± SD, n=6 for all.

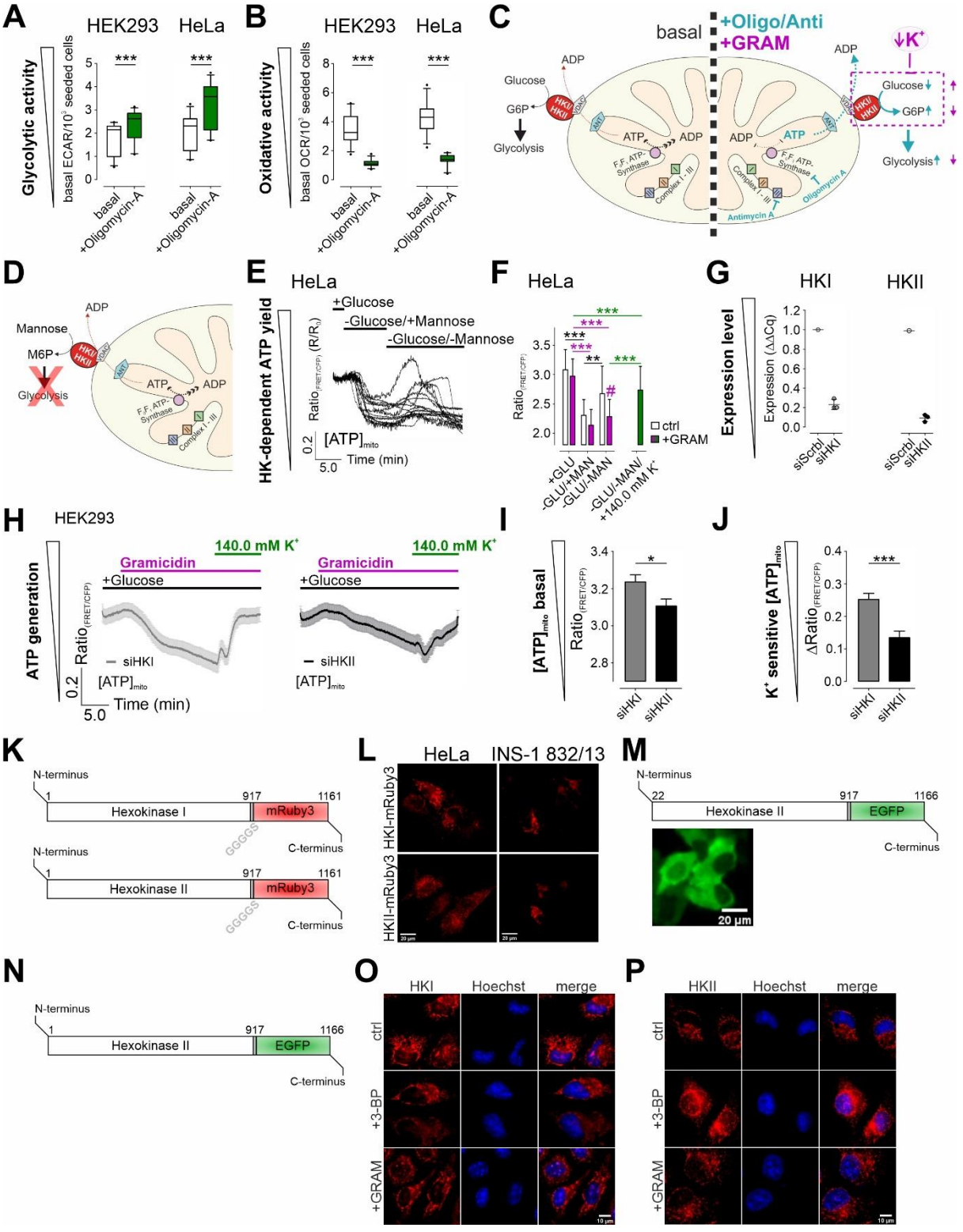

Figure S4. HKII status determines K^+ sensitivity of cell metabolism, related to Figure 4 and Figure 5. (A, B) ECAR/10^3 seeded cells levels (**A**) and OCR/10^3 seeded cells (**B**) of HEK293 (left panels) and HeLa cells (right panels), either under basal conditions (basal, white boxes) or of the same cells after treatment with 2 µM oligomycin-A (+Oligomycin-A, green boxes). n=4 for all. ***p≤0.001, (**A**) Wilcoxon matched-pairs signed rank test or (**B**) Paired t-test (HEK293) and Wilcoxon matched-pairs signed rank test (HeLa). (**C**) Scheme demonstrating the first and essential step in glycolysis under basal (left), or under oligomycin-A and antimycin-A (+Oligo/Anti, cyan, right) ± gramicidin (+GRAM, magenta, right) treated conditions. (**D**) Scheme demonstrating the effect of mannose treatment on glycolysis in HeLa cells. After mannose uptake, the hexose sugar is phosphorylated to mannose-6-phosphate (M6P) by mitochondria-associated HKs, thereby consuming ATP from the mitochondrial matrix. M6P is, however,

not further utilized in glycolysis in these cells. (**E**) Single cell $[ATP]_{mito}$ responses of HeLa cells in response to mannose treatment. 10.0 mM glucose were substituted for mannose, or both hexose sugars were removed as indicated. n=4. (**F**) FRET-ratio signals of control (ctrl, white bars) or gramicidin treated HeLa cells (+GRAM, magenta and green bars) expressing mtAT1.03, either under basal conditions (+GLU), upon glucose to mannose substitution (-GLU/+MAN) and after removal of both (-GLU/-MAN). The green bar shows the FRET-ratio signal of gramicidin treated HeLa cells in the absence of both substrates upon addition of 140.0 mM K^+ (-GLU/-MAN/+140.0 mM K^+). Bars show average ± SD. Statistics correspond to the panels (**E**) and **Fig.4C**. Statistical analysis was performed either using Friedman test followed by Dunn's MC test (ctrl) or Repeated Measures One-Way ANOVA test with Geisser-Greenhouse correction, followed by Tukey's MC test (+GRAM). **p≤0.01, ***p≤0.001. #p≤0.05 using Unpaired t-test for comparison of ctrl and +GRAM under the same condition. n=4 for both. (**G**) Quantification of HKI (left) and HKII expression (right) ± SD in HEK293 cells using qPCR analysis upon cell treatment with a control siRNA (siScrbl, white circles) or siRNA against HKI (siHKI, light grey circles, left) or HKII (siHKI, dark grey circles, right), respectively. n=3 for all. (**H**) $[ATP]_{mito}$ over-time of HEK293 cells either treated with siRNA against HKI (siHKI, left panel, grey curve) or siRNA against HKII (siHKII, right panel, black curve) in response to cell treatment with 15 µM gramicidin in the absence of K^+, followed by re-addition of 140.0 mM K^+. Data represent average ± SEM, n=4 independent experiments for siHKI, n=3 independent experiments for siHKII. (**I, J**) Statistics correspond to (**H**) and demonstrate the basal FRET-ratio signal of HEK293 cells expressing mtAT1.03, either treated with siHKI (grey bars) or siHKII (black bars) (**I**), or the ΔFRET-ratio signal of mtAT1.03 upon administration of gramicidin in the absence of K^+, respectively (**J**). Bars show average ± SEM. n=4 for siHKI, n=3 for siHKII, *p≤0.05 using Unpaired t-test and ***p≤0.001 using Mann-Whitney test. (**K**) Schematic illustration of HKI-mRuby3 (upper scheme) and HKII-mRuby3 (lower scheme). N- and C-terminus, amino acid positions, and flexible linkers (GGGGS) are indicated. (**L**) Representative fluorescence wide-field images of HeLa (left images) and INS-1 832/13 cells (right images) either expressing HKI-mRuby3 (upper images) or HKII-mRuby3 (lower images). Scale bars show 20 µm. (**M**) Upper panel shows a schematic illustration of truncated HKII-EGFP (trHKII-EGFP), lacking the first 21 amino acids responsible for mitochondrial binding of HKII. N- and C-terminus and amino acid positions are indicated. The lower panel demonstrates representative fluorescence wide-field images of HeLa cells expressing trHKII-EGFP. Scale bar shows 20 µm. (**N**) Schematic illustration of HKII-EGFP. N- and C-terminus and amino acid positions are indicated. (**O, P**) Representative immunofluorescence wide-field images of HeLa cells stained for HKI (red, left images, **O**) or HKII (red, left images, **P**) in combination with Hoechst for nuclear staining (blue, middle images, **O** and **P**). Right images represent overlays of HKI and Hoechst (**O**) or HKII and Hoechst (**P**). HeLa cells were either not treated (ctrl, upper images, **O** and **P**) or treated with 3-BP (middle images, **O** and **P**) or gramicidin (lower images, **O** and **P**) for 15 minutes. Scale bar in the lower right images represents 10 µm. n=3 for all conditions.

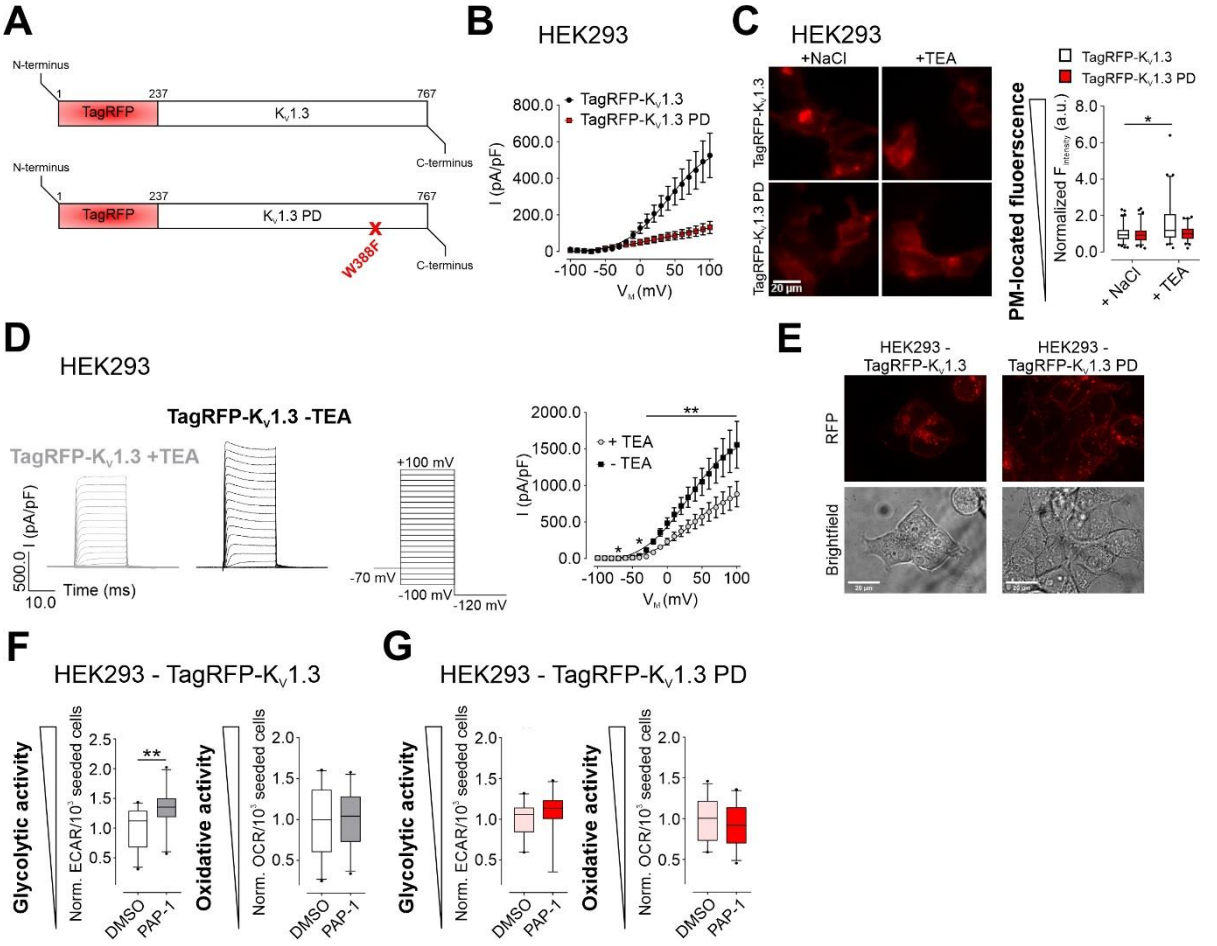

Figure S5. Physiologic consequences of altered K^+ homeostasis on cell metabolism, related to Figure 6. (**A**) Schematic representation of TagRFP-K_V1.3 (upper) and TagRFP-K_V1.3 PD (lower) bearing a W388F mutation indicated by the red X. (**B**) Current-voltage (IV) curves for TagRFP-K_V1.3 (black circles) and TagRFP-K_V1.3 PD (red squares). Data represent average ± SEM and were fitted using Boltzmann sigmoidal function. V_{50} was determined as 40.60 mV (9.066 mV – 72.13 mV) for TagRFP-K_V1.3 and 46.28 mV (-107.90 mV – 200.40 mV) for TagRFP-K_V1.3 PD, respectively. n=13 HEK293 cells for TagRFP-K_V1.3 and n=12 HEK293 cells for TagRFP-K_V1.3 PD. (**C**) Representative fluorescence wide-field images (left) and quantification of plasma membrane-located fluorescence (right) in HEK293 cells either expressing TagRFP-K_V1.3 (upper images and white boxes) or TagRFP-K_V1.3 PD (lower images and red boxes). Images were acquired using 40x magnification. Cells were either cultivated in the presence of 15 mM NaCl (+NaCl, left images and boxes) or 15 mM tetraethylammonium chloride (+TEA, right images and boxes). Scale bar represents 20 µm. (**D**) Representative currents (left) and IV curves (right) of HEK293 cells expressing TagRFP-K_V1.3, either in the presence (TagRFP-K_V1.3, +TEA, grey curves and circles) or absence of TEA (TagRFP-K_V1.3 -TEA, black curves and circles). Currents were evoked by voltage steps as demonstrated. Data in the right panel represent average ± SEM and were fitted using Boltzmann sigmoidal function. V_{50} was determined as 34.34 mV (16.66 mV – 74.90 mV) in the presence of TEA and 29.00 mV (11.16 mV – 121.20 mV) after TEA wash-out. Statistical analysis was performed either using Paired t-test (-80 mV, -70 mV, -40 mV) or Wilcoxon matched-pairs signed rank test (for all other voltages). *p≤0.05, **p≤0.01. n=9 cells. (**E**) ACLSM fluorescence (upper images) and bright-field images (lower images) of HEK293 cells either stably expressing TagRFP-K_V1.3 (left images) or TagRFP-K_V1.3 PD (right images). Scale bars represent 20 µm. (**F**) Normalized ECAR/10^3 (left) and OCR/10^3 (right) seeded HEK293 cells stably expressing TagRFP-K_V1.3, either in the presence of DMSO (DMSO, white boxes) or PAP-1 (PAP-1, grey boxes), in the absence of extracellular K^+. **p≤0.001, Unpaired t-test. n=3. (**G**) Normalized ECAR/10^3 (left) and OCR/10^3 (right) seeded HEK293 cells stably expressing TagRFP-K_V1.3 PD, either in the presence of DMSO (DMSO, light red boxes) or PAP-1 (PAP-1, dark red boxes), in the absence of extracellular K^+. p=0.1083 for ECAR and p=0.2086 for OCR, Mann-Whitney test. n=3.

Transparent Methods

Buffers, solutions, and media

Buffers used for fluorescence time-lapse imaging comprised:
Cell equilibration buffer (in mM): 2 $CaCl_2$, 10 D-glucose, 10 HEPES, 5 KCl, 2 L-glutamine, 0.44 KH_2PO_4, 1 $MgCl_2$, 135 NaCl, 2.6 $NaHCO_3$, 0.34 Na_2HPO_4, with 1X MEM amino acids and 1X MEM vitamins added. pH was adjusted to 7.45 using NaOH.
Cytosol like buffer containing (in mM): 10 D-glucose, 0.1 EGTA, 10 HEPES, 110 KCl, 10 $MgCl_2$, 10 NaCl, pH adjusted to 7.45 with NaOH and HCl. If ions (Ca^{2+}, K^+, Mg^{2+} or Na^+) were added or removed, NMDG in the same amount was used for osmolarity maintenance. EGTA was absent in Ca^{2+} containing buffer.
0 mM K^+ buffer containing (in mM): 2 $CaCl_2$, with or without 10 D-glucose or D-mannose as indicated in the panels, 10 HEPES, 1 $MgCl_2$, 143 NaCl, pH adjusted to 7.45 with NaOH. In experiments where TEA was used, 15 mM of NaCl was replaced for 15 mM of TEA for osmolarity maintenance. If not otherwise stated in the panels, 0 mM K^+ buffer containing 2 mM $CaCl_2$ and 10 mM D-glucose was used for imaging experiments.
140.0 mM K^+ buffer containing (in mM): 2 $CaCl_2$, with or without 10 D-glucose or D-mannose as indicated in the panels, 10 HEPES, 140 KCl, 1 $MgCl_2$, pH adjusted to 7.45 with KOH.
To receive buffers containing different [K^+], 0 mM K^+ buffer and 140.0 mM K^+ buffer were mixed in appropriate portions.
For imaging experiments, gramicidin at a consistent concentration of 15 µM was used. Mitochondrial depolarization was performed using 3 µM oligomycin-A and 5 µM antimycin-A. 3-BP treatment was performed at a concentration of 300 µM. Ionomycin, nigericin, and monensin were used at a concentration of 3 µM, 5 µM, and 10 µM, respectively.

Media used for extracellular flux analysis using the Seahorse device (Agilent Technologies California, US) comprised:
SM-Na (LK) medium was composed of (in mM): 1.8 $CaCl_2$, 0.000248 $FeCl_2$, 0.814 $MgSO_4$, 115.36 NaCl, 44 $NaHCO_3$ and 0.908 NaH_2PO_4, with 0.5% phenol red solution, 1X MEM amino acids and 1X MEM vitamins added. Freshly, before measurements (in mM) 2 L-glutamine, 5.5 D-glucose, and 1 sodium pyruvate were added and pH was adjusted to 7.40 with NaOH.
SM-K (HK) medium was composed of (in mM): 1.8 $CaCl_2$, 0.000248 $FeCl_2$, 115.36 KCl, 44 $KHCO_3$, 0.908 KH_2PO_4 and 0.814 $MgSO_4$, with 0.5% phenol red solution, 1X MEM amino acids and 1X MEM vitamins added. Freshly, before measurements (in mM) 2 L-glutamine, 5.5 D-glucose, and 1 sodium pyruvate were added and pH was adjusted to 7.40 with KOH.

Buffers used for NMR sample preparation comprised:
DPBS-Na (LK) was composed of (in mM): 0.9 $CaCl_2$, with or without 10 D-glucose or $^{13}C_6$-D-glucose, 0.5 $MgCl_2$, 138 NaCl, 1.47 NaH_2PO_4, 15.3 Na_2HPO_4, with or without 0.005 PSSS, pH adjusted to 7.45 with NaOH.
DPBS-K (HK) was composed of (in mM): 0.9 $CaCl_2$, with or without 10 D-glucose or 10 $^{13}C_6$-D-glucose, 138 KCl, 1.47 KH_2PO_4, 15.3 K_2HPO_4, 0.5 $MgCl_2$, pH adjusted to 7.45 with KOH.
NMR buffer containing (in mM): 80 Na_2HPO_4, 5 3-(trimethylsilyl) propionic acid-2,2,3,3-d4 sodium salt (TSP) and 0.04% (w/v) NaN_3, all compounds were dissolved in D_2O and pH was adjusted to 7.40 with NaOH and HCl.

Oligonucleotides and Plasmids

Primers used for qPCR analysis and cloning were purchased from Thermo Fisher Scientific. siRNAs used for knockdown of HKI or HKII were purchased from Santa Cruz Biotechnology (Texas, US). Scrambled siRNA was purchased from Microsynth AG (Vienna, Austria) with the following sequence: 5'–UUCUCCGAACGUGUCACGUTT–3'.
Plasmid encoding for mitochondrial-targeted ATP sensor was a gift from Hiromi Imamura at Kyoto University, Kyodai Graduate School of Biostudies, Japan.
Plasmids encoding for other genetically encoded probes except K^+ biosensors and K_V1.3 variants were purchased from Addgene: HKI-mRuby3 and HKII-mRuby3 were *de novo* synthesized and purchased from Gene Universal (Delaware, US).

Cloning and DNA purification

Cloning of TagRFP-K_V1.3 and TagRFP-K_V1.3 PD was performed using conventional PCR-, restriction- and ligation-based cloning. pGEX-MK3 served as a PCR template. For amplification of wild-type K_V1.3, ClaI-K_V1.3 fwd. and HindIII-K_V1.3 rev. primers were used. K_V1.3 W388F fwd. in combination with HindIII-K_V1.3 rev. and ClaI-K_V1.3 for., in combination with K_V1.3 W388F rev. primers were used to introduce the point mutation W388F in pGEX-MK3 (K_V1.3). PCRs were performed using Herculase II fusion DNA polymerase according to manufacturer's instructions. PCR reactions were controlled using a 1.5% agarose gel. PCR products showing the proper size after electrophoresis were cut and purified using the Wizard SV Gel and PCR Clean-Up System. The two fragments bearing the W388F mutation were used for another PCR with ClaI- K_V1.3 for. and HindIII K_V1.3 rev. primers to receive the full-length product (K_V1.3 PD) bearing a point mutation (W388F), followed by agarose gel electrophoresis and gel DNA extraction. Subsequently, purified PCR products of full-length K_V1.3 and K_V1.3 PD, and a pcDNA3.1(-) vector containing TagRFP were used for restriction using ClaI and HindIII according to manufacturer's instructions, followed by ligation using T4 DNA ligase. The ligated products were transformed into chemically competent 10-beta bacteria using the supplied protocol and spread on agar-agar plates containing 100 µg mL-1 ampicillin,

followed by incubation at 37°C over-night. The next day, colonies were picked, transferred into 5 mL of LB-medium with 100 µg mL-1 ampicillin added, and bacteria were cultured over-night at 37°C vigorously shaking, followed by plasmid minipreps using the Monarch Plasmid Miniprep Kit. Clones were sent for sequencing (Microsynth AG) for verification.
DNA Maxiprep's of plasmids were performed by culturing bacteria containing the respective plasmid in 500 mL LB-media, either with 100 µg mL-1 ampicillin or 50 µg mL-1 kanamycin, depending on the plasmid, over-night. The next day, plasmid DNA was extracted using the 15 NucleoBond Xtra Maxi kit according to manufacturer's instructions.

In vitro HK activity assay

The activity of recombinant purified HKI and HKII *in vitro* was determined using a colorimetric HK activity assay kit. To investigate thermal inactivation of HKI and HKII, 40 µL of assay buffer containing a final concentration of recombinant purified HKs of 4.0 ng/µL were incubated at 37°C for 1.5 hours. Determination of HK activities was performed using an absorbance plate reader (Infinite F200 Pro, TECAN, Männedorf, Switzerland). An average of $\Delta absorbance_{10min}$ over 1 hour was generated, and data were normalized to condition without additional K^+ added for representation.

In silico 3D modelling

3D structure of HKI and HKII were generated using the PyMol Molecular Graphics System, Version 2.0 Schrödinger, LLC., based on the crystallographic models of Rosano et al. (RCSB accession number 1QHA) for HKI and Nawaz et al. (RSCB accession number 2NZT) for HKII (Nawaz et al., 2018; Rosano et al., 1999). One asymmetric unit of the crystal structure was chosen and represented as a cartoon model in grey. Amino acids known to generate K^+ binding structures including asparagine, aspartate, glutamine, and glutamate were colored in blue. Unidentified atoms found in the crystallographic model of HKII are represented as red spheres.

Cell culture and transfection

HEK293, HeLa, MCF-7, and MDA-MB-453 cells (all purchased from ATCC, Virginia, US) were cultivated in DMEM (Thermo Fisher Scientific) complemented with 10% FCS, 1 mM sodium pyruvate, 100 U mL^{-1} penicillin-streptomycin, and 2.5 µg mL^{-1} amphotericin B. INS-1 832/13 cells were a gift from C.B. Newgard (Department of Pharmacology and Cancer Biology, Duke University School of Medicine, USA) and were cultivated in GIBCO RPMI 1640 medium additionally supplemented with 10% FCS, 10 mM HEPES, 1 mM sodium pyruvate, 0.05 mM 2-mercaptoethanol, 100 U mL^{-1} penicillin-streptomycin and 2.5 µg mL^{-1} amphotericin B. All cell lines were cultivated in a humidified incubator at 37°C with 5% CO_2. HEK293, HeLa, MCF-7 and MDA-MB-453 cells were retrieved from female organisms. INS-1 832/13 cells were retrieved from a male organism. HeLa cells were authenticated by STR analysis. All other cell lines were not authenticated.

For transfection, either PolyJet *in vitro* DNA transfection reagent (SignaGen Laboratories, Maryland, US) or TransFast transfection reagent (Promega GmbH) were used according to manufacturer's instructions.

Extracellular flux analysis

Assessment of OCR and ECAR levels was performed using a Seahorse-XFe96 Analyzer (Agilent Technologies). For analysis of wild-type cells, cells were seeded one day before the experiment in the respective cell culture medium using the following cell numbers: 70,000, 50,000, 100,000, 50,000, and 80,000 cells for HEK293, HeLa, INS-1 832/13, MCF-7, and MDA-MB-453 cells, respectively. Cells were cultivated over-night in a humidified incubator at 37°C and 5% CO_2. The next day, cells were removed from the incubator and washed 2X with SM-Na (LK) or SM-K (HK) medium, prior SM-Na/K medium containing 5 µM gramicidin (1:3,000 from DMSO stock) or 0.033% DMSO was added. Subsequently, cells were incubated at ambient environment at 37°C for 20 minutes, 5 µM gramicidin or 0.033% DMSO containing medium was removed and replaced for the respective SM-Na/SM-K medium, followed by a 10-minute incubation phase at 37°C. Next, cells were analyzed using the Seahorse-XFe96 Analyzer (Agilent Technologies).

For analysis of ECAR- and OCR levels under conditions of mitochondrial inhibition, oligomycin-A at a final concentration of 2 µM (1:1,000 from DMSO stock) was injected. Either ECAR/OCR ratio was calculated, or ECAR and OCR raw values were normalized for the seeded cell numbers.

For extracellular flux analysis of HEK293 cells stably expressing TagRFP-K_V1.3 or TagRFP-K_V1.3 PD, cells originally cultivated in the presence of 1 µM PAP-1 (1:10,000 from DMSO stock) were pelleted at 200 rcf at room temperature for 5 minutes, the supernatant was removed, cells were resuspended in complemented DMEM without PAP-1 and re-pelleted at 200 rcf at room temperature for 5 minutes. Again, the supernatant was removed, cells were resuspended in fresh complemented DMEM without PAP-1 and were seeded at 70.000 cells per well in complemented DMEM, either in the presence of 1 µM PAP-1 (1:10,000 from DMSO stock) or equivalent amounts of DMSO (0.01%). Cells were cultivated over-night in a humidified incubator at 37°C in the presence of 5% CO_2. The next day, cells were removed from the incubator and washed 1X with SM-Na (LK) or SM-K (HK) medium with 1 µM PAP-1 (1:10,000 from DMSO stock) or equivalent levels of DMSO (0.01%), respectively. Subsequently, cells were incubated in an ambient environment at 37°C for 30 minutes and cells were analyzed using the Seahorse-XFe96 Analyzer (Agilent Technologies). ECAR as well as OCR values were normalized for the seeded cell number, or ECAR/OCR levels were calculated. All data were analyzed using Seahorse Wave Desktop Software (Agilent Technologies) and Microsoft Excel software (Microsoft, New Mexico, US).

Determination of the K^+ sensitivity of $[ATP]_{mito}$ and $[GLU]_{cyto}$

EC_{50} of $[ATP]_{mito}$ for K^+ was assessed using HEK293 cells expressing mtAT1.03. Analysis was performed using an fluorescence microscope as specified in the "Wide-field fluorescence time-lapse imaging" section. Experiments were started in the presence of 140.0 mM K^+ buffer followed by gramicidin administration. Subsequently, $[K^+]$ was reduced to 1.0 mM K^+ as indicated in the panels. For analysis, normalized FRET-ratio, i.e. $[ATP]_{mito}$, was plotted over the respective $[K^+]$ present in the extracellular buffer.

EC_{50} of $[GLU]_{cyto}$ for K^+ was assessed using HEK293 cells expressing FLII^{12}Pglu-700µδ6. Therefore, 30.000 HEK293 cells were seeded per well of a black 96-well cell culture microplate with transparent bottom two days before the experiment. After 24 hours, cells were transfected with FLII^{12}Pglu-700µδ6 using PolyJet transfection reagent according to manufacturer's instructions. The next day, media was removed, cells were washed once with 0 mM K^+ buffer, followed by an incubation for 20 minutes with buffers containing different $[K^+]$ received from mixing 0 mM K^+ buffer and 140.0 mM K^+ buffer in appropriate portions, and 15 µM gramicidin. After 20 minutes, FRET-ratio signals were analyzed using the CLARIOstar fluorescence plate-reader (BMG Labtech, Ortenberg, Germany). For analysis, the normalized FRET-ratio, i.e. $[GLU]_{cyto}$, was plotted over the respective $[K^+]$ present in the extracellular buffer.

Metabolite quantification using NMR

For NMR-experiments, HEK293, HeLa, and INS-1 832/13 cells were cultivated in 10 cm dishes using the respective culture medium. At a confluence of ~80% the medium was removed, and cells were washed with DPBS-Na/DPBS-K medium containing 10 mM D-glucose and 5 µM PSSS for extracellular K^+ removal. Subsequently, cytosolic glucose of cells was depleted by changing medium to DPBS-Na/DPBS-K without D-glucose, with 5 µM PSSS added. After an incubation phase of 5 minutes, DPBS-Na/DPBS-K medium without D-glucose and without PSSS, either containing 15 µM gramicidin (1:1,000 from DMSO stock) or 0.1% DMSO were added, and after 5 minutes cell supernatant was exchanged for the same medium. After another 15 minutes, DPBS-Na/DPBS-K containing $^{13}C_6$-labelled glucose was added for 20 minutes and 0.5 mL of supernatant was collected for later analysis. Cells were quickly washed 1X with DPBS-Na/DPBS-K medium without D-glucose and without $^{13}C_6$-labelled glucose, media was removed, 0.5 mL of ddH2O was added, cells were scraped using cell scrapers and the lysate was transferred into 2.0 mL reaction tubes. For protein removal and to quench enzymatic reactions in the samples, the 0.5 mL of each sample was mixed with 1.0 mL of methanol, and samples were homogenized using a precellys homogenizer. Both, media and cell pellets, were stored at -20°C for 1 hour until further processing. Afterwards, the samples were spun at 17949 rcf at 4°C for 30 minutes. Supernatants were lyophilized and 0.5 mL of NMR buffer was added to the samples and transferred to 5 mm NMR tubes. All NMR

experiments were performed at 310 K on an AVANCE™ Neo Bruker Ultrashield 600 MHz spectrometer equipped with a TXI probe head and processed as described previously (Alkan et al., 2018). The 1D CPMG (Carr-Purcell_Meiboom_Gill) pulse sequence (cpmgpr1d, 512 scans, 73728 points in F1, 11904.76 Hz spectral width, 128/512 transients for media/cell extracts, recycle delays 4 s) with water suppression using pre-saturation, was used for ^{1}H 1D NMR experiments. Bruker Topspin version 4.0.2 was used for NMR data acquisition. The spectra for all samples were automatically processed (exponential line broadening of 0.3 Hz), phased, and referenced using TSP at 0.0 ppm using Bruker Topspin 4.0.2 software (Bruker GmbH, Rheinstetten, Germany). Spectra pre-processing and data analysis have been carried out using the state-of-the-art data analysis pipeline proposed by the group of Prof. Jeremy Nicholson at Imperials College London using Matlab® scripts and MetaboAnalyst 4.0 (Chong et al., 2018). NMR data were imported to Matlab® vR2014a (Mathworks, Natick, Massachusetts, United States), regions around the water, TSP, and remaining methanol signals excluded, and probabilistic quotient normalization (Dieterle et al., 2006) was performed to correct for sample metabolite dilution. To identify changes in metabolic profiles, multivariate statistical analysis was performed as described previously(Huber et al., 2019) and includes Principle Component Analysis (PCA), Orthogonal-Partial Least Squares - Discriminant Analysis (O-PLS-DA) (Maher et al., 2008), and all associated data consistency checks and 7-fold cross-validation. Stated concentrations correspond to normalized concentrations after probabilistic quotient normalization.

Wide-field fluorescence time-lapse imaging

Prior to experiments, all cells were equilibrated for at least 30 minutes in cell equilibration buffer. Time-lapse imaging experiments of cells was performed either using an Olympus IX73 inverted microscope (Olympus, Vienna, Austria) with a 40X objective (UApo N 340, 40X/1.35 Oil, ∞/0.17/FN22, Olympus), or a Zeiss Axiovert.A1 FL (Zeiss, Oberkochen, Germany) equipped with a 40X objective (Objectiv Fluar, 40X/1,30 Oil M27, Zeiss). Both microscopes were connected to an OMICRON LedHUB High-Power LED Light Engine for illumination, equipped with a 455 nm and either a 530 nm or a 505-600 nm LED light source (OMICRON electronics, Vienna, Austria). Excitation filters were as follows: 427/10 nm and 575/15 (AHF Analysentechnik, Tübingen, Germany), respectively. Emission of FRET-sensors was detected at 475 and 530 nm, respectively, and emissions were either separated using a photometrics DV2 image splitter (Teledyne Technologies Inc., Arizona, US), or an Optosplit II image splitter (Teledyne Technologies Inc.), both equipped with a T505lpxr (AHF Analysentechnik) . Images were captured at a binning of 4, either using a Retiga R1 CCD-camera (TELEDYNE QIMAGING, Surrey, Canada) attached to the Olympus IX73, or a pco.panda 4.2 bi sCMOS-camera (PCO, Kelheim, Germany) attached to the Zeiss Axiovert.A1 FL. Buffer exchange and cell stimulation during data acquisition were performed using the PC30 perfusion chamber

(NGFI GmbH, Graz, Austria) connected to a gravity-based perfusion system (NGFI GmbH). For data analysis, raw fluorescence over-time values were exported to Microsoft Excel software (Microsoft) corrected for the background, and FRET-ratio values were generated

High-resolution confocal imaging

Array Confocal microscopy was performed using an array confocal laser scanning microscope (ACLSM) built on a fully automatic inverse microscope (Axio Observer.Z1, Zeiss) using a 100X objective (Plan-Apochromat 100X, 1.4 Oil M27, Zeiss). Microscope was equipped with a Yokogawa CSU-X1 Nipkow spinning disk system and a piezoelectric z-axis motorized stage. Laser light of diode lasers (Visitron Systems) served as excitation light source: GFP of HKII was excited using a 488 nm laser light, mRuby3 of HKI and TagRFP-K_V1.3 variants was excited using 561 nm laser light. Emissions were captured at 516 nm and 644 nm, respectively. The VisiView Premier Acquisition software (Visitron Systems, Puchheim, Germany) was used for image acquisition and microscope control. Buffer exchange and cell stimulation during data acquisition was performed using the PC30 perfusion chamber (NGFI GmbH) connected to a gravity-based perfusion system (NGFI GmbH). Image representation of ACLSM images and analysis of cytosolic HKII-GFP/HKI-RFP ratio was performed using ImageJ and Microsoft Excel software.

qPCR analysis

Expression levels of HKI and HKII were assessed on day 2 after siRNA transfection. RNAs were isolated using the peqGOLD total-RNA kit and cDNA was generated using the High-Capacity cDNA Reverse Transcription Kit according to manufacturer's instructions. qRT-PCR was performed using the GoTaq qPCR Kit on a LightCycler 480 (Roche Diagnostics, Vienna, Austria). Relative expression of specific genes was normalized to α-Tubulin as a housekeeper.

Generation of HEK293 cells stably expressing TagRFP-K_V1.3 or TagRFP-K_V1.3 PD

HEK293 cells were transfected with respective plasmids using PolyJet transfection reagent. 48 hours after transfection, G418 at a final concentration of 500 µg μL^{-1} was added. After 5 days of cell cultivation in the presence of G418, cells were detached, sorted by FACS (FACS Aria IIIu, BD Biosciences, Heidelberg, Germany) for red fluorescence (excitation at 561 nm, emission 586/15 nm) and mixed cell populations of each K_V1.3 variant were cultivated.

Immunofluorescence staining and quantification

On day of fixation, cells were washed 2X with PBS, and fixed using a 50/50 mixture of -18°C cooled methanol/ acetone followed by washing 3X with PBS and addition of the blocking buffer (5% BSA in PBS) for 2 hours mildly shaking. Subsequently, primary antibodies (Mouse monoclonal anti-α-Tubulin, RRID: AB_1904178, Rabbit monoclonal anti-Hexokinase I, RRID: AB_2116996, Rabbit monoclonal anti-Hexokinase II, RRID: AB_2232946) were added to the

cells in PBS with 5% BSA. Cells were incubated over-night at 4°C. On the next day, primary antibody solutions were removed, cells were washed 3x with blocking buffer and secondary antibody solution containing Goat anti-Mouse IgG1 Cross-Adsorbed Secondary Antibody, Alexa Fluor 488 (RRID: AB_2535764) and Goat anti-Rabbit IgG (H+L) Cross-Adsorbed Secondary Antibody, Alexa Fluor 555 (RRID: AB_2535849) at a dilution of 1:2,500 were added. Cells were incubated for 2 hours in the dark at room temperature. Finally, cells were washed 3X with PBS, and mounted using PermaFluor Aqueous Mounting Medium with 1 µg mL^{-1} Hoechst 33342 added. Images were acquired using a Zeiss Axiovert.A1 FL equipped with a 40X objective (Objectiv Fluar, 40X/1,30 Oil M27, Zeiss). For illumination, an OMICRON LedHUB High-Power LED Light Engine equipped with a 385 nm, 475 nm, and 505-600 nm LED (OMICRON electronics), and 380x, 473/10, and 575/15 excitation filters (all from AHF Analysentechnik), was used.

For investigation of endogenous HKI and HKII localizations upon 3-BP or gramicidin treatment, cells were treated at room temperature with 500 µM 3-BP or 15 µM gramicidin in 0 mM K^+ buffer for 15 minutes prior to fixation.

Patch-clamp recordings

Recordings were performed in whole-cell mode. Currents were evoked by 21 voltage square pulses (20 ms each) from -70 mV holding potential to voltages between -100 mV and +100 mV delivered in 10 mV increments. Voltages were corrected off-line for the capacity referring to the surface of the plasma membrane. The pipette solution contained (in mM): 0.05 EGTA, 10 HEPES, 110 K-Aspartate, 30 KF, 1 $MgCl_2$ and 10 NaCl, pH adjusted to 7.20 with KOH. For amplifier control and data acquisition, Patchmaster software (HEKA Elektronik GmbH, Lambrecht, Germany) was used. Data analysis was performed using Fitmaster software (HEKA Elektronik GmbH), Nest-o-Patch software (http://sourceforge.net/projects/nestopatch, written by Dr. V Nesterov), and Microsoft Excel (Microsoft).

Statistical analysis

Statistical analysis was performed using Prism5 software (GraphPad). Data were tested for Gaussian distribution using D'Agostino and Pearson omnibus normality test. Either a two-tailed Unpaired t-test or a two-tailed Mann-Whitney test was used for pairwise comparison of non-paired observations. For pairwise comparison of paired observations, either a Paired t-test or Wilcoxon matched-pairs signed rank test was used. Comparison of >2 data sets was done either using One-way ANOVA followed by Tukey's multiple comparison (MC) test, Repeated Measures ANOVA followed by Tukey's MC test, Kruskal-Wallis test followed by Dunn's MC test or Friedman test followed by Dunn's MC test. The statistical test is indicated in the figure legends. p-values of ≤0.05 were indicated with *, p≤0.01 with **, and p≤0.001 with ***. No sample size estimation was performed.

KEY RESOURCES TABLE

REAGENT or RESOURCE	SOURCE	IDENTIFIER
Antibodies		
Goat anti-Mouse IgG1 Cross-Adsorbed Secondary Antibody, Alexa Fluor 488	Thermo Fisher Scientific	Cat#A-21121; RRID: AB_2535764
Goat anti-Rabbit IgG (H+L) Cross-Adsorbed Secondary Antibody, Alexa Fluor 555	Thermo Fisher Scientific	Cat#A-21428; RRID: AB_2535849
Mouse monoclonal anti-α-Tubulin	Cell Signaling Technology	Cat#3873S; RRID: AB_1904178
Rabbit monoclonal anti-Hexokinase I	Cell Signaling Technology	Cat#2024S; RRID: AB_2116996
Rabbit monoclonal anti-Hexokinase II	Cell Signaling Technology	Cat#2867S; RRID: AB_2232946
Bacterial and Virus Strains		
NEB 10-beta Competent *E.coli* (High Efficiency)	New England Biolabs	Cat# C3019I
Chemicals, Peptides, and Recombinant Proteins		
2-Mercaptoethanol	Sigma Aldrich	Cat#M6250
3-bromo-2-oxopropionic acid (3-BP)	Sigma Aldrich	Cat#16490
5-(4-Phenoxybutoxy)psoralen (PAP-1)	Sigma Aldrich	Cat#P6124
$^{13}C_6$-D-Glucose	Sigma Aldrich	Cat#389374
50x MEM Amino Acids Solution	Thermo Fisher Scientific	Cat#11130051
100x MEM Vitamin Solution	Thermo Fisher Scientific	Cat#11120052
100x Sodium Pyruvate Solution	Thermo Fisher Scientific	Cat#11360070
Acetone	Carl Roth	Cat#5025
Advanced RPMI 1640 Medium	Thermo Fisher Scientific	Cat#12633012
Agarose	VWR International	Cat#732-2789
Amphotericin B	Thermo Fisher Scientific	Cat#15290018
Ampicillin Sodium Salt	Sigma Aldrich	Cat#A9518
Antimycin-A	Abcam	Cat#ab141904
Agar-Agar Kobe I	Carl Roth	Cat#5210
Bovine Serum Albumin (BSA)	Carl Roth	Cat#8076
$CaCl_2$ $2H_2O$	Carl Roth	Cat#5239
Carbonyl cyanide 4-(trifluoromethoxy)phenylhydrazone (FCCP)	Santa Cruz Biotechnology	Cat#sc-203578
Cytochalasin-B	Sigma Aldrich	Cat#C6762
D-Glucose H_2O	Carl Roth	Cat#6887
DMEM, high Glucose, HEPES	Thermo Fisher Scientific	Cat#12430054
Ethyleneglycol- bis(β-aminoethyl)-N,N,N',N'-tetraacetic Acid (EGTA)	Carl Roth	Cat#3054
$FeCl_2$	Sigma Aldrich	Cat#372870
Fetal Calf Serum	Thermo Fisher Scientific	Cat#26140
G418	Sigma Aldrich	Cat#A1720
GoTaq qPCR Kit	Promega	Cat#A6001
Gramicidin	Sigma Aldrich	Cat#G5002
HEPES	Carl Roth	Cat#9105
Herculase II Fusion DNA Polymerase	Agilent	Cat#600677
High-Capacity cDNA Reverse Transcription Kit	Thermo Fisher Scientific	Cat#4368814
Hoechst 33342	Thermo Fisher Scientific	Cat#62249
Ionomycin Free Acid	Tocris	Cat#2092
Kanamycin Sulfate	Sigma Aldrich	Cat#K1377

K-Aspartate	Sigma Aldrich	Cat#A6558
KCl	Carl Roth	Cat#6781
KF	Sigma Aldrich	Cat#2617
$KHCO_3$	Carl Roth	Cat#X887
K_2HPO_4	Carl Roth	Cat#T875
KH_2PO_4	Carl Roth	Cat#P018
KOH	Carl Roth	Cat#P747
$MgCl_2\,6H_2O$	Carl Roth	Cat#A537
Methanol	Carl Roth	Cat#AE71
Monarch Plasmid Miniprep Kit	New England Biolabs	Cat#T1010S
Monensin Sodium Salt	Tocris	Cat#5223
NaCl	Carl Roth	Cat#9265
$NaHCO_3$	Carl Roth	Cat#0965
Na_2HPO_4	Carl Roth	Cat#P030
NaH_2PO_4	Carl Roth	Cat#T878
NaOH	Carl Roth	Cat#6771
Nigericin Sodium Salt	Tocris	Cat#4312/10
N-Methyl-D-Glucamine (NMDG)	Sigma Aldrich	Cat#M2004
NucleoBond Xtra Maxi Kit for Transfection-Grade Plasmid DNA	Macherey-Nagel	Cat#740414.10
Oligomycin-A	Tocris	Cat#4110/5
Penicillin-Streptomycin (10,000 U/mL)	Thermo Fisher Scientific	Cat#15140122
PermaFluor Aqueous Mounting Medium	Thermo Fisher Scientific	Cat#12695925
peqGOLD Total-RNA Isolation Kit	VWR	Cat#12-6634-01
Phenol Red Solution	Sigma Aldrich	Cat#P0290
Phosphate Buffered Saline	Thermo Fisher Scientific	Cat#10010023
PolyJet *In Vitro* DNA Transfection Reagent	SignaGen Laboratories	Cat#SL100688
Poly(sodium 4-Styrenesulfonate) (PSSS)	Sigma Aldrich	Cat#243051
Recombinant Hexokinase-I	Abcam	Cat#ab85918
Recombinant Hexokinase-II	Abcam	Cat#ab85920
T4 DNA Ligase	New England Biolabs	Cat#M0202S
Tetraethylammonium Chloride (TEA)	Sigma Aldrich	Cat#T2265
TransFast Transfection Reagent	Promega	Cat#E2431
Triton-X 100	Carl Roth	Cat#3051
Trypsin-EDTA (0.5%)	Thermo Fisher Scientific	Cat# 15400054
Trypton/Pepton	Carl Roth	Cat#8952
Wizard SV Gel and PCR Clean-Up System	Promega	Cat#A9281
Yeast Extract	Carl Roth	Cat#2904
Critical Commercial Assays		
Hexokinase Colorimetric Assay Kit	Sigma Aldrich	Cat#MAK091
Experimental Models: Cell Lines		
HEK293	ATCC	Cat#CRL-1573
HEK293 cells stably expressing TagRFP-K_V1.3 (HEK293 TagRFP-K_V1.3)	This paper	N/A
HEK293 cells stably expressing TagRFP-K_V1.3 PD (HEK293 TagRFP-K_V1.3 PD)	This paper	N/A
HeLa	ATCC	Cat#CCL-2

INS-1 832/13	Gift from C.B. Newgard (Department of Pharmacology and Cancer Biology, Duke University School of Medicine, USA)	N/A
MCF-7	ATCC	Cat#HTB-22
MDA-MB-453	ATCC	Cat#HTB-131
Oligonucleotides		
ClaI-K_V1.3 forward 5'–GTCATCGATATGACCGTGGTGCCCGGG–3',	This paper	N/A
HindIII-K_V1.3 reverse 5'–GCTAAGCTTAGACATCAGTGAATATCTTCTTG–3'	This paper	N/A
K_V1.3 W388F forward 5'-GATGCCTTCTTTTGGGCAGTAG-3'	This paper	N/A
K_V1.3 W388F rev.: 5'–TGGTTACTACTGCCCAAAAGAAG –3'	This paper	N/A
qPCR HKI forward 5'-TGGTGGCTGTGGTCAACGACAC-3'	This paper	N/A
qPCR HKI reverse 5'-TTCATCTCCTCCATGTAGCAGGC-3'	This paper	N/A
qPCR HKII forward 5'-GAGAGGACTTTGACATGGATGTGG-3'	This paper	N/A
qPCR HKII reverse 5'-CAATGCCTGCTACATGGAG-3'	This paper	N/A
qPCR Tubulin forward 5'-CCATGGTAAATACATGGCTTG-3'	This paper	N/A
qPCR Tubulin reverse 5'-CAACCTTGAAGCCAGTGG-3'	This paper	N/A
scrbl siRNA 5'–UUCUCCGAACGUGUCACGUTT–3'	This paper	N/A
siRNA against HKI	Santa Cruz Biotechnology	Cat#sc-39044
siRNA against HKII	Santa Cruz Biotechnology	Cat#sc-35621
Recombinant DNA		
AMPKAR	Addgene	Cat#35097; RRID: Addgene_35097
FLHKI-pGFPN3	Addgene	Cat#21917; RRID: Addgene_21917
HKI-mRuby3	This paper	N/A
HKII-mRuby3	This paper	N/A
Laconic/pcDNA3.1(-)	Addgene	Cat#44238; RRID: Addgene_44238
mt lc-LysM GEPII 1.0	Next Generation Fluorescence Imaging	Cat#mt lc-LysM GEPII 1.0
mtAT1.03	Imamura et al.	10.1073/pnas.0904764106
NES lc-LysM GEPII 1.0	Next Generation Fluorescence Imaging	Cat#NES lc-LysM GEPII 1.0
pcDNA3.1 FLII12Pglu-700μδ6	Addgene	Cat#17866; RRID: Addgene_17866
pGEX-MK3	Addgene	Cat#30188; RRID: Addgene_30188
TagRFP-K_V1.3	This paper	N/A
TagRFP-K_V1.3 PD	This paper	N/A
TrHKII-pGFPN3	Addgene	Cat#21921; RRID: Addgene_21921

Software and Algorithms		
Excel Office 365	Microsoft	https://www.office.com/
Fitmaster	HEKA Elektronik	https://www.heka.com/
ImageJ	Schneider et al., 2012	https://imagej.nih.gov/ij/
Matlab	MathWorks	https://www.mathworks.com/products/matlab.html
MetaboAnalyst 4.0	Wishart Research Group, University of Alberta	https://www.metaboanalyst.ca/
Nest-o-Patch	Written by Dr. V. Nesterov	http://sourceforge.net/projects/nestopatch
Patchmaster	HEKA Elektronik	https://www.heka.com/
Prism 8	GraphPad	https://www.graphpad.com/scientific-software/prism/
PyMol	Schrödinger	https://pymol.org/2/
Seahorse Wave Desktop Software	Agilent	https://www.agilent.com/en/product/cell-analysis/real-time-cell-metabolic-analysis/xf-software/seahorse-wave-desktop-software-740897
VisiView	Visitron Systems	https://www.visitron.de/products/visiviewr-software.html

Supplemental References

Alkan, H.F., Walter, K.E., Luengo, A., Madreiter-Sokolowski, C.T., Stryeck, S., Lau, A.N., Al-Zoughbi, W., Lewis, C.A., Thomas, C.J., Hoefler, G., et al. (2018). Cytosolic Aspartate Availability Determines Cell Survival When Glutamine Is Limiting. Cell Metabolism *28*, 706-720.e6.

Chong, J., Soufan, O., Li, C., Caraus, I., Li, S., Bourque, G., Wishart, D.S., and Xia, J. (2018). MetaboAnalyst 4.0: towards more transparent and integrative metabolomics analysis. Nucleic Acids Research *46*, W486–W494.

Dieterle, F., Ross, A., Schlotterbeck, G., and Senn, H. (2006). Probabilistic Quotient Normalization as Robust Method to Account for Dilution of Complex Biological Mixtures. Application in ^{1}H NMR Metabonomics. Anal. Chem. *78*, 4281–4290.

Huber, K., Hofer, D.C., Trefely, S., Pelzmann, H.J., Madreiter-Sokolowski, C., Duta-Mare, M., Schlager, S., Trausinger, G., Stryeck, S., Graier, W.F., et al. (2019). N-acetylaspartate pathway is nutrient responsive and coordinates lipid and energy metabolism in brown adipocytes. Biochimica et Biophysica Acta (BBA) - Molecular Cell Research *1866*, 337–348.

Maher, A.D., Crockford, D., Toft, H., Malmodin, D., Faber, J.H., McCarthy, M.I., Barrett, A., Allen, M., Walker, M., Holmes, E., et al. (2008). Optimization of Human Plasma ^{1}H NMR Spectroscopic Data Processing for High-Throughput Metabolic Phenotyping Studies and Detection of Insulin Resistance Related to Type 2 Diabetes. Anal. Chem. *80*, 7354–7362.

Nawaz, M.H., Ferreira, J.C., Nedyalkova, L., Zhu, H., Carrasco-López, C., Kirmizialtin, S., and Rabeh, W.M. (2018). The catalytic inactivation of the N-half of human hexokinase 2 and structural and biochemical characterization of its mitochondrial conformation. Bioscience Reports *38*, BSR20171666.

Rosano, C., Sabini, E., Rizzi, M., Deriu, D., Murshudov, G., Bianchi, M., Serafini, G., Magnani, M., and Bolognesi, M. (1999). Binding of non-catalytic ATP to human hexokinase I highlights the structural components for enzyme–membrane association control. Structure *7*, 1427–1437.

Update

iScience

Volume 24, Issue 5, 21 May 2021, Page

DOI: https://doi.org/10.1016/j.isci.2021.102468

iScience

CellPress
OPEN ACCESS

Correction

Potassium ions promote hexokinase-II dependent glycolysis

Helmut Bischof,* Sandra Burgstaller, Anna Springer, Lucas Matt, Thomas Rauter, Olaf A. Bachkönig, Tony Schmidt, Klaus Groschner, Rainer Schindl, Tobias Madl, Nikolaus Plesnila, Robert Lukowski, Wolfgang F. Graier, and Roland Malli*

*Correspondence: helmut.bischof@uni-tuebingen.de (H.B.), roland.malli@medunigraz.at (R.M.)

https://doi.org/10.1016/j.isci.2021.102468

(iScience *24*, 102346-1–102346-13; April 23, 2021)

During the revision process, we regret that a version of the manuscript was submitted without the key resource table in the transparent methods section of the supplemental data. It was therefore not included in the manuscript at publication. The key resource table has now been added to the supplemental pdf as it is indispensable for reproducing the study. The authors apologize for the mistake and any inconvenience this has caused.